Self-assembled epitaxial growth of CdSe quantum dot structures

Martin Bartels

Paderborn, December 2003

Self-assembled epitaxial growth of CdSe quantum dot structures

Von der Fakultät für Naturwissenschaften
der Universität Paderborn
zur Erlangung des akademischen Grades eines

Doktor der Naturwissenschaften

genehmigte

Dissertation

von

Martin Bartels

Paderborn, Dezember 2003

Abstract

The semiconductor system CdSe/ZnSe is a promising candidate for the fabrication of optoelectronic devices in the blue and blue-green spectral range. The exchange of conventional two-dimensional structures by zero-dimensional structures (Quantum Dot Structures QDS) in the active layer of the device can overcome the disadvantages of the structural properties of the II-VI semiconductors (degradation).

With Molecular Beam Epitaxy (MBE) up to three monolayers (MLs) of CdSe are deposited on a ZnSe layer. Cd-rich inclusions (type A-islands) with diameters of 5 nm form inside of the CdSe wetting layer. The density of the type A-islands (10^{11}cm^{-2}) shows no dependence on the CdSe coverage, whereas the Cd-content increases with the deposition.

CdSe-islands with diameters of 16 nm are formed in a self-organized Stranski-Krastanow (SK) growth process (type B-islands or SK-islands). The density of the type B-islands increases with the CdSe coverage, whereas the Cd-content (90%) shows no dependence on the deposition.

The formation process of both island classes is investigated by using different substrates and varying the growth parameters. The type A-islands can be avoided by use of vicinal substrates (6°) or under metal-rich growth conditions. For the type B-islands a growth window of 2-3 MLs CdSe coverage was found. With less CdSe, the formation process does not occur, a larger coverage results in relaxation of the CdSe layer with formation of stacking faults.

By replacing the stabilizing selenium atmosphere with a sulphur atmosphere, i. e. formation of CdS instead of CdSe, the lattice mismatch of -7.5% is reduced to -3.9%. The fully strained type B-islands degenerate, which shows the reversibility of the SK growth process in the system CdSe/ZnSe.

Photoluminescence (PL) investigations on bimodal QDS reveal that the type A-islands dominate the luminescence up to T=100 K. At higher temperatures redistribution processes of excitons into type B-islands occur. An energetic redshift of the maximum of the PL signal of ~170 meV is characteristic for bimodal QDS. This redshift is significantly larger than the one of ZnSe (~60 meV) within the same temperature range. However, structures exposed to a sulphur atmosphere (i. e degeneration of type B-islands) show a redshift with increasing temperature of ~60 meV.

Investigations on 10fold stacks of CdSe type B-islands show the importance of excitons localized in QD ensembles. QD structures on both, exact oriented and vicinal substrates show optical gain up to 300 cm^{-1}, which enables the use of these structures as active layer in laser diodes (LD).

Contents

1 Introduction

One of the most important optoelectronic devices is the solid state or semiconductor laser diode (LD). The field of application goes from optical data transfer over optical mass storage devices, Compact-Disc player and writer, printer to indicators, sensors and so on.

However, up to now, there is still no real solution for a laser diode operating between 450 nm and 600 nm. Whereas GaN is a compromising candidate for the blue spectral range (440 nm – 500 nm), so ZnSe may be a suitable solution for the green to yellow spectral range (500 nm – 560 nm).

In 1991 the first blue-green LD with pulsed operation at T=77 K was presented by 3M [Haas91]. In 1997 Sony presented a LD which had an operating time of more than 100 hours in continuous wave (cw) mode [Naka97]. Eagle-Pitcher, USA [Easo95] sells ZnSe-based light emitting devices (LEDs) with operating times of around 8000 hours and Kato et al [Kato98] presented a ZnCdSe based LD with operating times of 400 hours at room temperature.

All these researches in the early 90ies resulted in nearly perfect mastery of epitaxy of these compound semiconductors by Molecular Beam Epitaxy (MBE), with fabrication of layers of highest structural perfection [Land95].

In fact, the concurrent system GaN gathers more importance, this is due to material based advantages of the nitride-semiconductors as, e. g. a higher structural stability. To overcome the relative fast degradation of ZnSe based LDs which is due to the low activation energy for the formation of dislocations and the gliding into the active layer, two different ways are followed.

1. "Hardening" of the II-VI materials with Beryllium compounds by maintaining the typical quantum well (QW)-structure [Waag97].
2. Replacing the two-dimensional quantum well structures by zero-dimensional quantum dot (QD)-structures in the active layer of the device.

The reduction of the dimension of the optical active layer leads to a larger binding energy of the excitons and a larger oscillator strength of the localized states, due to a higher coulomb interaction within the quantum dots. This should result in a reduction of the current threshold density of the LDs and has been reported for the system InAs/GaAs quantum dots [Grun96]. Herein the current threshold density could be reduced by an order of magnitude compared with conventional quantum well diodes. Additionally the thermal stress in the device is reduced, too. Gerald et al [Gera96] reported a spatial separation of the localized states and the defects of the structure. By the replacement of quantum wells by quantum dots, the mechanism for the degradation would be of minor importance. This all indicates that a reduction in dimension of the active layer, some of the disadvantages based on material properties can be compensated and optical efficient and long living devices can be realized.

Concerning the strong localization of excitons in the system CdSe/ZnSe two structurally different morphologies of QDs have to be distinguished. On the one hand there are coherently strained three-dimensional islands of CdSe (type B), which are embedded in a ZnSe matrix. These structures are grown in a Stranski-Krastanow (SK)-mode [Flac96, Leon97, Merz98, Rabe98] in analogy to the system InAs/GaAs. On the other hand there is a strong localization of excitons in quasi two-dimensional areas with Cd composition fluctuations (type A) [Stra98a]. These structures show excitonic and biexcitonic gain at high excitation densities.

This work concentrates on the growth process for bimodal QD structures. Chapter 2 describes the SK-growth mode and gives an overview on the parameters of the used materials (ZnSe, CdSe, CdS). In chapter 3 the equipment for the MBE system is described and also the different MBE growth modes. The morphology of the two different size classes is handled in chapter 4. The differences of the fluctuation islands (type A-islands) compared with the SK-grown islands (type B-islands) are shown. The reversibility of the formation process of these type B-islands indicates its thermodynamical character. Chapter 5 covers the optical properties of the bimodal quantum dot ensembles and the influence of a sulphur exposition on the CdSe quantum dots. The grown structures are also suitable for single dot spectroscopy, which is described in chapter 6. Optical gain and stimulated emission, which is necessary for laser applications is discussed in chapter 7 and finally the results are summarized in chapter 8.

2 Self-assembled formation of QDs

2.1 Material systems: ZnSe, CdSe and CdS

On top of an epiready GaAs substrate almost perfect ZnSe layers have been grown in a two stage MBE system. To understand the growth process some basic information on the used materials must be explained. ZnSe crystallizes in the zincblende crystal structure, which is shown in figure 2.1. Although CdSe crystallizes in a wurzite crystal structure under equilibrium conditions, a metastable zincblende structure is grown on top of zincblende ZnSe. Some physical properties, like lattice parameter or bandgap energy are listed in table 2.1 for the semiconductors ZnSe, CdSe, CdS, GaAs and InAs.

Table 2.1: Physical properties for the different semiconductor materials ZnSe, CdSe, CdS, GaAs and InAs. [Land80].
(*) Only an average m_h^* is given.

	ZnSe	CdSe	CdS	GaAs	InAs
a_0 (300 K)	5.668 Å	6.052 Å	5.818 Å	5.653 Å	6.058 Å
E_g (2 K)	2.818 eV	1.765 eV		1.519 eV	0.411 eV
E_g (300 K)	2.713 eV	1.664 eV	2.50 eV	1.428 eV	0.354 eV
m_e^*	0.16 m_0	0.11 m_0	0.14 m_0	0.069 m_0	0.024 m_0
m_{hh}^*	0.78 m_0	0.44 m_0 (*)	0.51 m_0 (*)	0.50 m_0	0.41 m_0
m_{lh}^*	0.145 m_0			0.068 m_0	0.025 m_0
α $[10^{-6}K^{-1}]$	7.8	—	—	5.60	4.52

2.2 The different growth modes: FM, VW, SK

Basically, the growth of thin films is categorized into three types:

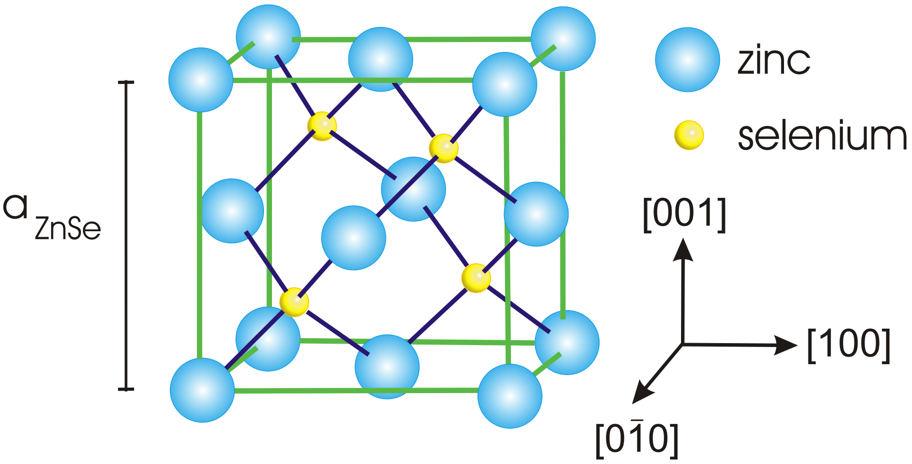

Figure 2.1: Zincblende crystal structure, i. e. fcc (face centered cubic) crystal structure. Each cell consists of 4 anions and 4 cations.

1. Frank-Van der Merwe (FM) [FvdM49]. The 2D layer-by-layer growth mode is observed for lattice-matched materials of identical crystal structure, i. e. Au on Ag, AlGaAs on GaAs.
2. Volmer-Weber (VW) [VoWe26]. Direct island growth is seen in materials with large lattice mismatch, high interfacial energy of different crystal structure, i. e. GaN on saphire and InAs on GaP.
3. Stranski-Krastanow (SK) [StKr37]. This type of growth occurs for crystals of dissimilar lattice parameters and low interfacial energy, like InAs on GaAs. After an initial layer-by-layer growth, islands form spontaneously, leaving a thin “wetting layer” underneath.

Figure 2.2 shows a comparism of the three different modes. For heteroepitaxial films of one material on substrates of another material, interface and volume free energies play an important role. J. Y. Tsao [Tsao93] proposed a description, where the relation between the free energy γ_E of the epitaxial layer, the free energy γ_S of the substrate surface and the free energy γ_I of the interface determines the equilibrium morphology of the growing film.

In case of

$$\gamma_E + \gamma_I < \gamma_S \tag{2.1}$$

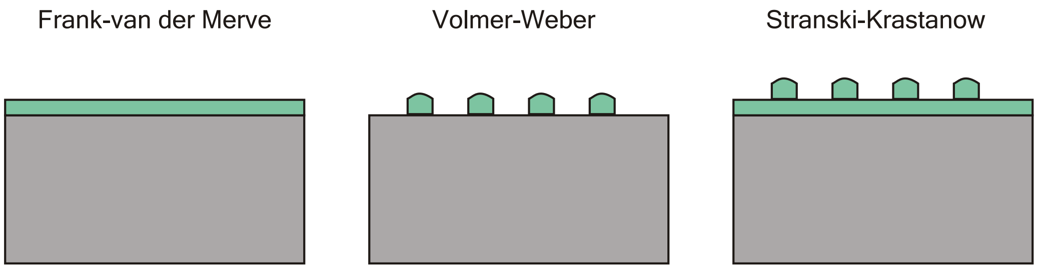

Figure 2.2: Scheme of the three different growth modes, Frank-van der Merwe (FM), Volmer-Weber (VW) and Stranski-Krastanow (SK).

the free energy of the system will be minimized, when the substrate surface is fully covered by the layer material. This leads to a two-dimensional growth, the Frank-van der Merwe growth mode.

The contradictory case

$$\gamma_E + \gamma_I > \gamma_s \tag{2.2}$$

means, the system minimizes the free energy, if the substrate layer is minimally covered, e. g. three-dimensional islands of the layer material are formed, which is the Volmer-Weber growth mode.

The conditions for the SK mode are more complex. Here the relation of the free energies is a function of the layer thickness d.

$$f(d) = \frac{\gamma_S - \gamma_E}{\gamma_I} \tag{2.3}$$

At the start of the material deposition, the same conditions as for the FM-mode are given, the wetting layer is formed.

$$\frac{\gamma_S - \gamma_I}{\gamma_E} > 1 \tag{2.4}$$

This wetting layer forms a new substrate and the relation of the free energies must be recalculated.

$$\frac{\gamma_{wet} - \gamma_{I_{wet}}}{\gamma_E} < 1 \tag{2.5}$$

Here, γ_{wet} is the free energy of the wetting layer as new built substrate and $\gamma_{I_{wet}}$ is the free energy of the interface between wetting layer and epilayer. This means, the preferred growth mode changes from two-dimensional to three-dimensional, which is typical for the SK mode. Instead of a pseudomorphic strained 2D layer, which can only relax in a direction perpendicular to the surface, most of the material is rearranged in 3D islands, while the rest remains in a thin, 2D wetting layer. With the appearance of these 3D islands, the strain situation changes fundamentally. A strain relief is formed within and around the islands which results in a decrease in the total free energy of the system.

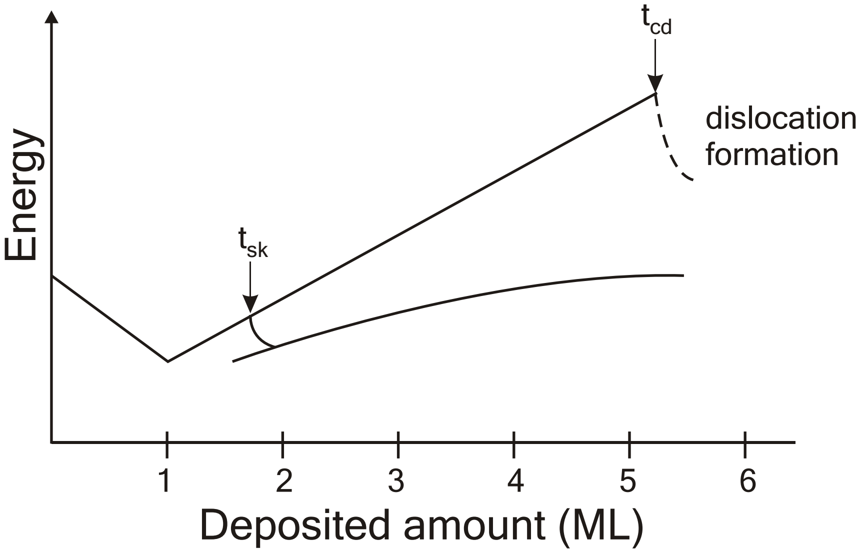

Figure 2.3: Free energy in dependence on the amount of deposited material for FM- and SK-growth modes [Seif96].

Figure 2.3 shows schematically the energetic situation for Frank-Van der Merwe morphology and Stranski-Krastanow morphology. In both cases, the depostition starts with a complete wetting layer on the substrate. Due to the energy contributions from the substrate and from the layer and due to changes in the surface energy of the different materials, the total energy of the system decreases until the substrate is fully covered by one monolayer. With further deposition the elastic energy E_{el} of an uniformly strained layer on a rigid substrate increases linearly in dependence on the layer thickness t in MLs.

$$E_{el} = \lambda \cdot \epsilon^2 \cdot A \cdot t \tag{2.6}$$

where λ is the elastic modulus, $\epsilon = \frac{\Delta a}{a}$ is the misfit and A is the surface area.

If the 2D FM growth mode is maintained, the elastic energy increases until it reaches the activation energy for formation of dislocations at t_{cd}. On the other hand, if the system is able to reduce the energy by formation of 3D islands and subsequent deformation of these islands, the system follows the path at t_{sk}. The difference in the total energy between the FM growth mode and the SK growth mode is given by:

$$\Delta E = \Delta E_{surf} + \Delta E_{el} \tag{2.7}$$

where ΔE_{surf} is the change in the surface energy and ΔE_{el} the change in the strain energy due to elastic relaxation. During the formation of the islands, the free surface increases, which increases the surface energy ΔE_{surf}. The energy gain of the system comes from the change of the elastic relaxation energy ΔE_{el} mainly due to elastic relaxation of the 3D islands.

2.3 Size limited growth of the SK islands

One of the fundamentals of the SK growth is the relative stability and the rather high uniformity in size and shape of the SK islands. This effect is caused by the strain distribution between the islands and the substrate.

SK growth is based on three conditions:

1. perfect wetting of the surface
2. increasing elastic misfit strain with increasing wetting layer thickness and
3. inhomogeneous elastic strain within each island as well as induced strain in the substrate after the appearance of the islands.

Strain and strain-relaxation is the thermodynamic driving force for coherent SK growth. The growth can be divided into three parts, the 2D deposition, the 2D-3D transition and the growth of the islands.

At the beginning, the deposition follows a layer-by-layer growth, which leads to a perfect wetting of the substrate. The elastic strain increases according to equation 2.6. At the critical thickness t_{sk} the stable 2D growth is left and an area of metastable 2D growth is entered. An excess energy E_e is stored within the pseudomorphically strained 2D layer, i. e. a supercritically thick wetting layer grows. The epilayer is ready to undergo a transition towards a SK morphology.

At a certain point, the excess energy E_e of the strained 2D layer reaches the energy of the 2D-3D transition barrier E_A and a 2D-3D transition becomes possible. However, at real growth temperatures, a thermally activated nucleation sets in before reaching this point. In a metastable strained 2D system with a critical thickness of t_{sk} MLs, any further deposition of material creates potential island nucleation sites. Thickness fluctuations lead to the formation of critical nuclei and the classical nucleation theories predict for the simplest case [Zink92]:

$$\frac{dN}{dt} = C \cdot \sigma \cdot \exp\left[-\frac{E_A - E_E}{kT}\right] \tag{2.8}$$

with σ: the supersaturation, i. e. the concentration of mobile excess material on the surface. With the creation of the first islands, E_e decreases due to partial strain relaxation. The islands grow and consume the material which is mobile enough to reach the nucleation sites. Assuming an exponential decrease of σ of the form $\sigma = \sigma_0 \cdot \exp\left(-kt^n\right)$, we get a simplified equation for a transient nucleation rate:

$$\frac{dN}{dt} = C \cdot \sigma_0 \cdot \exp\left(-kt^n\right) \exp\left[\frac{E_A - E_e}{kT}\right] \tag{2.9}$$

From equation 2.9 we see that, as soon as the first islands are formed, the nucleation will occur in a narrow time span due to:

1. the reduction in supersaturation and
2. the increase of the activation barrier for thermally activated nucleation.

The nucleation probability decreases quickly which determines the surface density of the dots. For higher nucleation densities, the strain-fields in the substrates surrounding the dots start to overlap. In this case dense arrays of dots will be formed [Shch95].

The last point is the growth of the islands. An important fact is the reason for "self-limited" growth and the decomposition of the 2D layer. As soon as the first stable nuclei have been formed, they start to decompose the supercritically thick wetting layer.

Figure 2.4 illustrates the strain energy density along the surface of the wetting layer and an island. The top of the island is the minimum in this potential, whereas the maximum

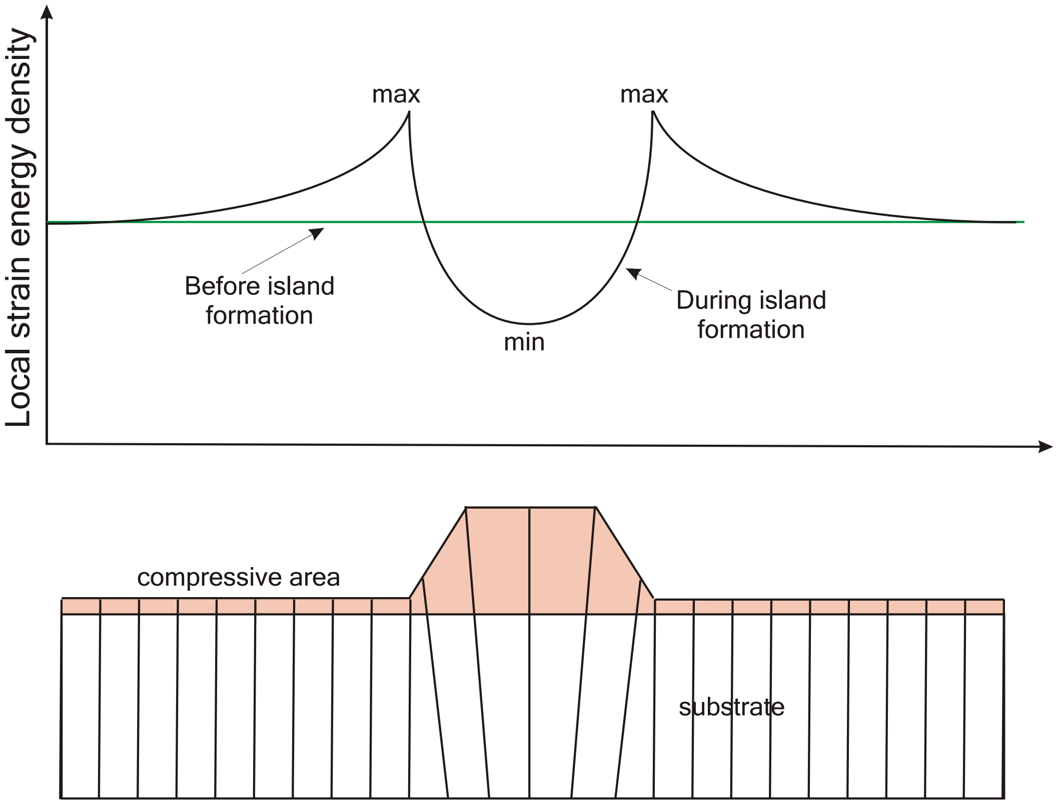

Figure 2.4: Local strain energy density before and during island formation as well as deformation of lattice planes due to strain in and around a 3D island [Seif96].

is at the edge of the island. The minimum is caused by the partial strain relaxation in the islands and this sink is the driving force for the material transfer to the island surface. The maximum on the other hand is caused by the high compressive strain at the edge of the island and its propagation along the substrate, which increases the misfit between substrate and wetting layer. In this model [Seif96], the exclusion zone around the island is determined by strain, whereas the depletion of material is a secondary effect.

The increase of the potential around the islands depends on the island size, which is why its formation has a self-limiting effect on the growth of the coherent islands. The potential acts as barrier for surface diffusion of material towards the island, therefore the growth of small islands is favoured and the growth of larger islands is inhibited.

3 MBE-System and growth procedures of CdSe quantum dots

3.1 Equipment of the MBE systems

The samples were grown in a two chamber MBE system. A III-V-MBE chamber, where GaAs was deposited on a substrate of the same material, was coupled via an ultra high vacuum transfer system with a second MBE chamber, where the II-VI materials were deposited.

The III-V system was equipped with a standard Knudsen effusion cell for the evaporation of gallium and with a cracker-cell for the evaporation of arsenic.

The II-VI system was equipped with standard effusion cells for the deposition of zinc and cadmium, as well as with a cracker-cell for the evaporation of selenium. Additionally there was an effusion cell for sulphur [Buda98] and a CARS25-RF plasma source (RF - Radio Frequency) for the generation of a highly excited hydrogen plasma. This was used for the deoxidation of the GaAs waver pieces in some of the experiments (see also section 3.4). All the cells can be opened and closed by moving a shutter into the molecular beam or out of the molecular beam.

Both systems are equipped with a RHEED (Reflection High Energy Electron Diffraction) system for the in-situ control of the layer growth and a temperature controlled substrate heater (PID controller). The fluxes of the cells, i. e. the BEP (Beam Equivalent Pressure) of the cells is measured by means of Bayard-Alpert ion gauges for reproducible conditions during different growth runs.

3.2 Growth processes of a CdSe quantum dot structure

3.2.1 Preparation of the sample

The MBE system described in section 3.1 is limited to sample pieces of a size of one inch in diameter. These pieces are glued onto a substrate holder (some block of molybdenum) with a compound of indium and gallium, which remains liquid at room temperature.

3.2.2 Deoxidation and growth of GaAs

The sample is transferred into the III-V-GaAs MBE system through a load lock chamber. Within a stationary arsenic atmosphere ($\sim 10^{-5} - 10^{-6}$ torr), the temperature of the sample is slowly increased. The sample surface is controlled by RHEED during the whole process of deoxidation and GaAs deposition.

After fully completed deoxidation, i. e. the reflexes of the GaAs crystal surface are visible under all azimuth angles, the Ga cell is opened additionally and the growth of GaAs is started. In most experiments, around 20 nm of GaAs are deposited, while the surface develops a clearly visible 2x4 reconstruction.

The quality of this surface is then checked with RHEED, i. e. RHEED intensity oscillations of the specular spot are monitored. From these oscillations, the Ga-flux and the thickness of the GaAs-layer can be determined. Typical RHEED oscillations (for ZnSe here) are shown in figure 3.1.

Afterwards the growth of GaAs is stopped by closing the Ga shutter. The substrate heater is turned off and the sample is cooled down under arsenic pressure. Now the sample is transferred under UHV-conditions (Ultra High Vacuum) into the II-VI MBE system.

3.2.3 Growth of ZnSe

Before transferring the sample with a well defined two-dimensional GaAs surface into the II-VI MBE system, some preparations have to be done. The chamber has to be "floated" with zinc, to reduce the selenium surplus in the remaining atmosphere in the system. This prevents the spontaneous formation of Ga_2Se_3, which is of hexagonal structure. If this happens, the sample is ruined, a cubic, two-dimensional growth of ZnSe will not be reached again. Finally all shutters have to be closed to transfer the sample into the system.

Under UHV conditions the sample is heated up to $T_S \approx 280\,^\circ C$. Monitoring the [110]-azimuth by RHEED, the initial procedure of ZnSe growth is started. At first, the zinc shutter, i. e. the zinc cell is opened for approximately ten seconds to increase the amount of zinc on the sample surface and reducing the possibility to form Ga_2Se_3. The next ten seconds the samples stays in vacuum, all the cells are closed. Afterwards, both the zinc and the selenium cells are opened simultaneously and the growth of ZnSe starts. This is monitored with the RHEED system. The oscillations of the intensity of the specular spot (fig. 3.1) of the ZnSe layer on the GaAs layer can be measured and used to calculate the growth rate of the ZnSe layer and the flux of the zinc cell (see also chapter 3.5). After growing 45 nm of ZnSe (i. e. 150 MLs), the zinc cell is closed, the sample remains under a selenium atmosphere, until the next step can be done, the growth of the CdSe layer, especially the formation of CdSe quantum dots.

3.2.4 Growth of CdSe quantum dots and wetting layer

There are at least two different procedures of growing CdSe and the formation of the type B-islands. At low substrate temperatures $\left(\sim 240\,^\circ C\right)$, the CdSe quantum dots are formed in an additional step after the deposition of the CdSe. At higher substrate temperatures $\left(\sim 330\,^\circ C\right)$ the quantum dots form during the deposition process. Both ways are described next.

Growing CdSe at lower substrate temperatures

A CdSe layer with a thickness between 2.1 MLs and 3.1 MLs is deposited on top of the ZnSe layer (see also chapter 4.2.3). The growth process is monitored by means of RHEED intensity oscillations of the specular spot in the [−110]-azimuth. The procedure is the same as for the ZnSe layer. At the end of the deposition the cadmium cell is closed and the layer remains under a selenium atmosphere. At lower substrate temperatures a highly strained two-dimensional wetting layer is formed. An increase of the substrate temperature increases the over-all energy of the system, which can be divided into surface energy and strain energy. The increase of the temperature is done by a step-by-step increase within several minutes. Figure 3.2 shows a typical temperature curve of the

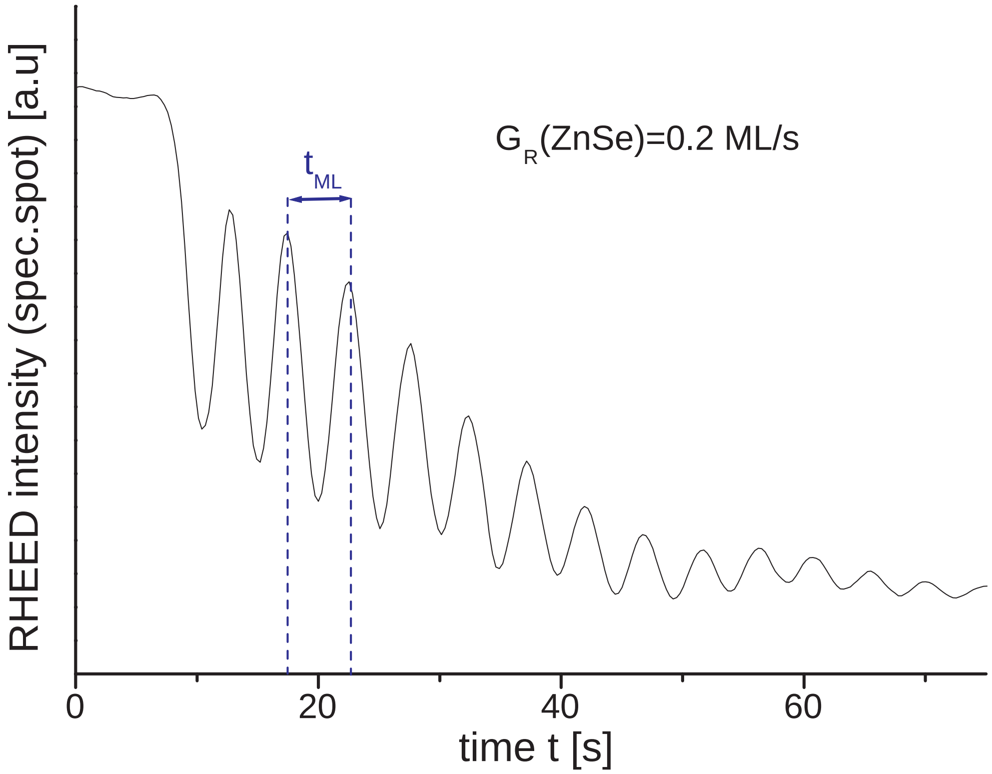

Figure 3.1: RHEED intensity oscillations of the specular spot at the beginning of the ZnSe growth on GaAs (001). The growth rate can be calculated by the distance of the maxima, i. e. the time needed for the growth of one monolayer. Also the flux of the zinc atoms can be calculated (see also 3.5).

substrate for this process.

At a sufficient substrate temperature, i. e. at a sufficient over-all energy, it becomes more preferable for the system to form three-dimensional islands with reduced strain than to remain two-dimensional. This phase change can be observed in-situ, the RHEED pattern changes significantly, additional 3D-reflexes occur, (-113) and (1-13). The 3D-QDs are then overgrown with a ZnSe layer.

Growing CdSe at higher substrate temperatures

Despite to the process in the previous section, CdSe may also be deposited at higher substrate temperatures. This results in the formation of the quantum dots during the growth process, just after exceeding a critical coverage of 2.1 MLs. As in the low temperature

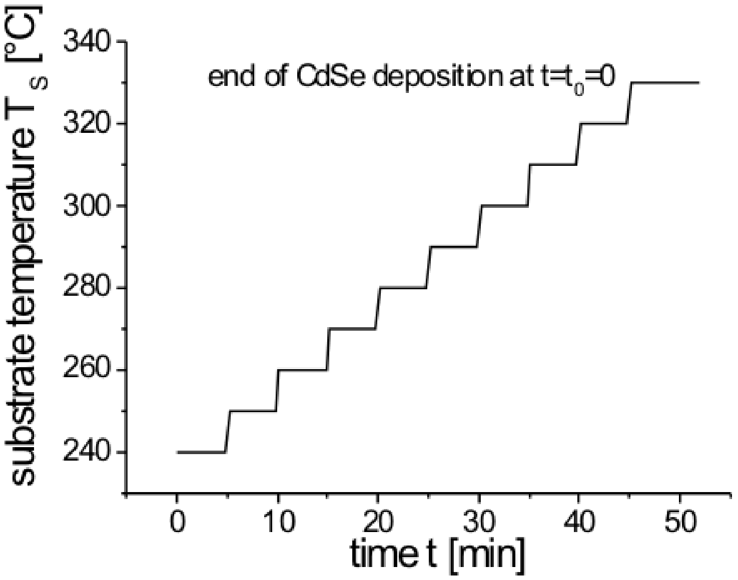

Figure 3.2: Temperature ramp for the formation of CdSe quantum dots.

case, the deposition of the CdSe can be monitored by RHEED intensity oscillations. Additionally, the transition from 2D (coverage less than 2.1 MLs) to a 3D surface (coverage more than 2.1 MLs) can be seen as there are 3D reflexes appearing in the RHEED pattern (compare figure 4.14c). Afterwards the 3D-QDs are overgrown with a ZnSe layer.

Exposing CdSe quantum dots to a sulphur atmosphere

In a series of experiments the CdSe quantum dots were exposed to an atmosphere of sulphur instead of selenium after formation. The aim of these experiments was to show the reversibility of the quantum dot formation, i. e. the reversibility of the Stranski-Krastanow process.

The exchange of the atmosphere is simply done by closing the selenium cell and simultaneously opening the sulphur cell. After the desired amount of sulphur exposure time, the process repeats vice versa. Immediately the opening of the zinc cell occurs to overgrow the formed layer with ZnSe.

3.3 Different growth methods

Three different growth modes have been used to grow the ZnSe buffer and cap layers. Figure 3.3 shows a scheme of the shutter states in Molecular Beam Epitaxy (MBE: a), Atomic Layer Epitaxy (ALE: b) and Migration Enhanced Epitaxy (MEE: c) growth mode.

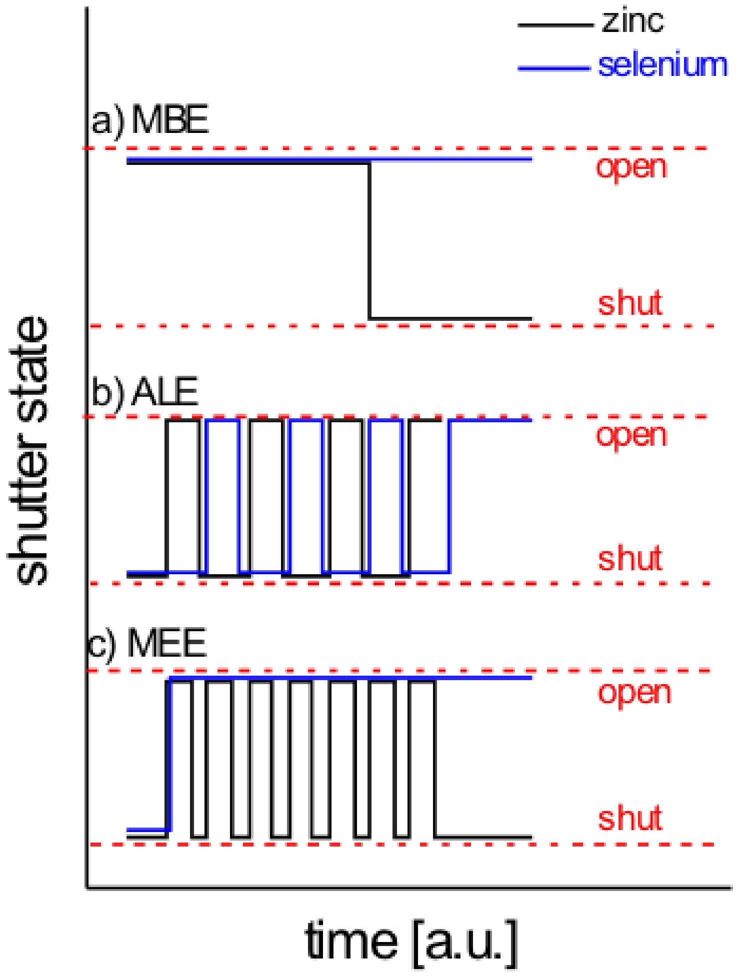

Figure 3.3: Shutter states for the different growth modes of ZnSe. (a) MBE, (b) ALE, (c) MEE.

3.3.1 Molecular Beam Epitaxy (MBE)

The MBE growth mode seems to be the "easiest" one to perform. All the cells with materials which are necessary to grow the desired semiconductor, are open at the same time. The layer in MBE mode grows continuously. To influence the growth of the desired material, it is possible to change the fluxes of the different molecular beams, i. e. to change the flux ratio of the metal and nonmetal element. In the case of ZnSe growth it is possible, to grow ZnSe under zinc rich, selenium rich or stoichiometric conditions. Figure 3.3a shows the states of the zinc and selenium shutter for a growth process in MBE mode.

3.3.2 Atomic Layer Epitaxy (ALE)

Growth in ALE mode means, that the cells open and close in an alternating sequence. Figure 3.3b shows this shutter sequence for growth of ZnSe in ALE mode. Between the closing of one shutter and the opening of the other one, both shutters remain closed for the time t_{delay}. This delay time is needed for the system to get back into an equilibrium like state which ensures that the growth conditions remain constant over a long time. Therefore, the opening time of the cells must be shorter than the growth time of one monolayer, otherwise on the surface of the substrate, clusters of the respective element are formed.

ALE growth of semiconductor materials not only takes much more time, it also makes high demands on the mechanical parts of the MBE system, i. e. the mechanics of the shutters. To give an example, we take a look on a typical sample with 45 nm ZnSe buffer layer and 45 nm ZnSe cap layer grown in ALE mode.

The lattice parameter of ZnSe is a=5.668 Å, so one monolayer is $d_{\mathrm{ML}} = \frac{1}{2} \cdot a = 2.834$ Å thick. To grow 45 nm of ZnSe we need approximately 150 MLs. The typical shutter sequence used to grow ZnSe in ALE mode is: 5 s zinc, 1 s delay time, 5 s selenium, 1 s delay time, i. e. 12 s per cycle. Two cycles are needed to grow one monolayer, so 300 cycles with 12 seconds each are needed to grow 150 MLs of ZnSe, that means 45 nm of ZnSe are grown in one hour in ALE mode. Growing in MBE mode with a typical growth rate of ZnSe of G_{R} (ZnSe) = 0.2ML/s, 45 nm of ZnSe need around 12.5 minutes to grow. ALE growth mode for ZnSe takes by a factor of six longer than in standard MBE mode (50 minutes longer for only the buffer layer, the cap layer takes again 50 minutes more).

On the other hand, there is the mechanical stress for the MBE system, the shutter of the zinc and the selenium cells have to open and to shut 300 times for the buffer layer and 300 times for the cap layer.

3.3.3 Migration Enhanced Epitaxy (MEE)

Migration Enhanced Epitaxy (MEE) differs from Atomic Layer Epitaxy (ALE), that the excess molecule cell is open all the time. In case of ZnSe growth, selenium is the excess material, i. e. the selenium cell remains open. The delay time is selected to enable the excess zinc atoms to reach favorable positions on the layer surface for an optimal two-dimensional growth process. The MEE growth mode is faster than the ALE mode. Because there is never a zinc rich surface, the grown layer does not roughen.

3.4 Deoxidation with an excited hydrogen-plasma

Some of the samples were deoxidized with an highly excited hydrogen plasma. The procedure took place in the II-VI MBE system under vacuum conditions, that means no selenium or zinc atmosphere were present. The sample is inserted onto the substrate manipulator and heated up to $T_S = 350\,^\circ C$. The hydrogen plasma is ignited and after around ten minutes the deoxidation of the GaAs takes place. This is monitored with the RHEED system. As soon as the GaAs-reflexes are visible in all azimuths, the Zinc cell is opened, the substrate is cooled down to $T_S \approx 300\,^\circ C$, the selenium cell is opened and the growth starts.

3.4.1 Ignition of the hydrogen plasma

The ignition parameters for the plasma source are approximately: Power (forward Power) P_{fw} =360 W and hydrogen flux f_{H_2} =0.5 sccm (sccm: standard cubic centimeter). Afterwards the needle valve at the cell is opened slowly until the pressure in the MBE system (normally $p = 2 \cdot 10^{-8}$ torr, monitored by the background Bayard-Alpert ion gauge) starts to increase. When the pressure reaches a value of about $p \approx 1 \cdot 10^{-5}$ torr the needle valve has to be closed slightly, the pressure will decrease and the plasma ignites between $p_{max} \approx 4.5 \cdot 10^{-6}$ torr and $p_{min} \approx 3.0 \cdot 10^{-6}$ torr. The regulation of the pressure is the tricky part of the ignition process because the pressure reacts very sensitive on the variation of the needle valve. Afterwards a pressure of $p_{\mathrm{deox}} \approx 3.5 \cdot 10^{-6}$ torr is set for the plasma deoxidation.

3.5 Calculation of the molecular flux

From the RHEED oscillations we can determine the growth rate G_R of ZnSe for example. As seen in fig. 3.1 on page 14 the growth rate of ZnSe is around G_R =0.2 ML/s. We can now calculate the atom flux for zinc. All we need is the time t_{ML} for the deposition of one monolayer and the number of zinc-atoms n_{Zn} in one cm^2 in one monolayer.

The lattice parameter of ZnSe is a_{ZnSe} =5.668 Å. According to that 1 cm^2 contains $3.113 \cdot 10^{14}$ atom cells. Comparing to fig. 2.1 on page 4, one monolayer is equivalent to the top layer of the lattice cube and includes two atoms (four on the corners, contributing each by a factor of $\frac{1}{4}$ and one in the middle of the cell). So we get the flux:

$$\mathrm{f_{Zn}} = \frac{\text{atoms per } cm^2}{\text{time per ML}} = \frac{\mathrm{n_{Zn}}}{\mathrm{t_{ML}}} = 2 \cdot \frac{3.113 \cdot 10^{14}}{5\,\mathrm{s} \cdot \mathrm{cm}^2} = 1.245 \cdot 10^{14} \frac{1}{\mathrm{s} \cdot \mathrm{cm}^2} \tag{3.1}$$

It must be mentioned, that the sticking coefficient was set to one. The sticking coefficient is the ratio of the number of absorbed atoms to the total number of impinging atoms. A sticking coefficient of one means, all the atoms on the surface are integrated into the growing layer, a sticking coefficient of 0.5 would mean, only every second atom is integrated into the growing layer.

3.6 Thickness variation

The previous section has shown that the growth rate of the layer depends on the flux and therefore on the impingement rate on the substrate surface. Due to the geometry of the MBE-system, this is not equal for the whole sample.

Figure 3.4 shows a scheme of the geometrical setup of the II-VI MBE system. One of the effusion cells is shown schematically, the other ones are only intimated by red crosses. Considering an ideal Knudsen effusion cell and the appropriate effusion behavior [HeSi89], the impingement rate dN is calculated for each point on the substrate by following equation:

$$\frac{\mathrm{dN}}{\mathrm{dr_{x,y}}} = \frac{\mathrm{r}_0^2}{\mathrm{r}_{\mathrm{x,y}}^2} \frac{\cos(\nu)}{\cos(\phi)} \cos(\nu + \phi) \quad \text{with} \tag{3.2}$$

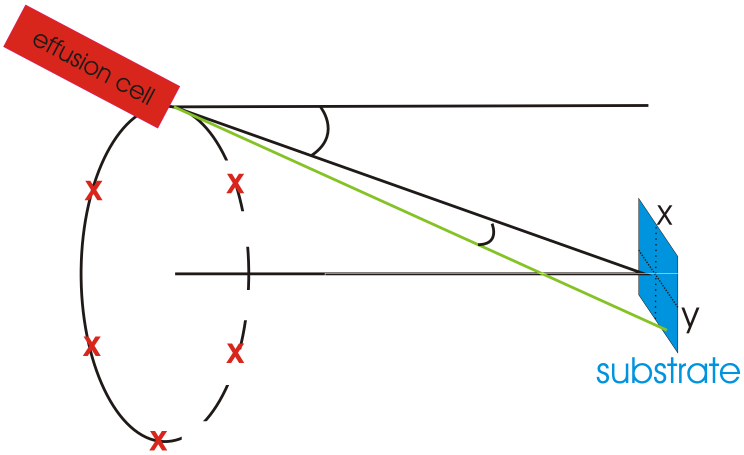

Figure 3.4: Schematic view of the cell geometry of the II-VI MBE system. The red arrows indicate the additional five effusion cells, which are all aligned on a circle around the substrate normal. x and y are the local coordinates on the substrate with the origin centered within.

dN : impingement rate normalized to the middle of the substrate
r_0 : distance from the effusion cell to the middle of the substrate
$r_{x,y}$: distance from the effusion cell to the point (x,y) on the substrate
ν : angle between cell axis and local point vector
ϕ : angle between substrate normal and cell axis

As an assumption, we assume that the effusion cell axis points onto the middle of the substrate. In the ideal case, i. e. $\phi = 0^\circ$ the impingement rate has a distribution with radial symmetry. The top of figure 3.5 displays this case and shows the relative layer thickness variation normalized to the middle of the substrate. For a typical sample size of 15 mm by 15 mm, the layer thickness differs only from d_0 in the middle to $0.9986 \cdot d_0$ in the corners of the sample.

For the real situation, i. e. $\phi = 20^\circ$ the layer thickness variation is no longer negligible, compare bottom of figure 3.5. The thickness differs from $1.02 \cdot d_0$ to $0.98 \cdot d_0$ from one side of the sample to the other one, which results in a relative variation of the thickness of 3% per millimeter on the sample. This leads unavoidable to a gradient in the coverage or thickness of CdSe, which has to be considered in a kinetic analysis of the SK-formation. We have found that the density of the type B-islands differs by an order of magnitude

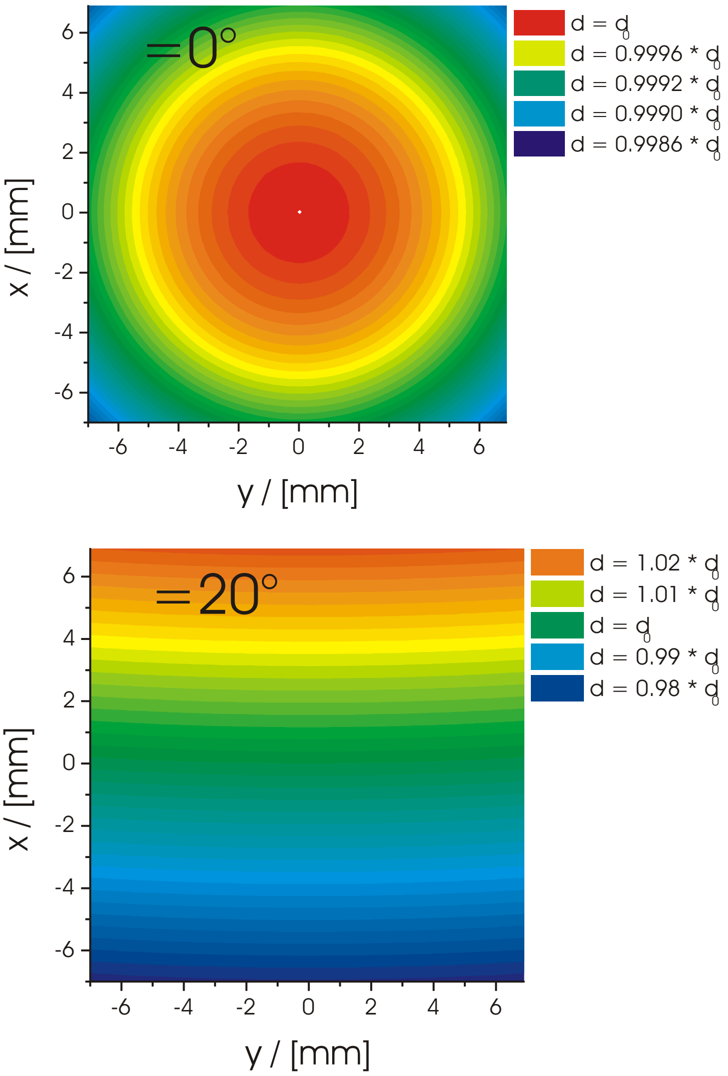

Figure 3.5: Layer thickness variation for ideal ($\phi = 0^\circ$) and real ($\phi = 20^\circ$) cell geometry. The thickness is normalized to d_0 in the middle of the sample, with x and y varying from -7 mm to +7 mm for a typical sample size.

(see also chapter 4.2.1) for samples with a size of 15 mm by 15 mm.

4 Structural properties of bimodal CdSe QD ensembles

To investigate a nucleation process, two different island distribution functions have been analyzed:

- The island density distribution function, which shows the density of 3D coherently strained islands in dependence on the amount of material deposited, i. e. coverage.
- The island size distribution function, which shows the size of 3D coherently strained islands in dependence of the coverage.

From the material parameters in table 2.1 on page 3, it is obvious that the material system CdSe/ZnSe has nearly the same lattice mismatch as the system InAs/GaAs, where Stranski-Krastanow grown islands have been reported [Gold85, Heit97a].

The lattice mismatch is defined as

$$\epsilon = \frac{a_S - a_L}{a_L} \tag{4.1}$$

For CdSe on ZnSe the lattice mismatch at $T_{\text{growth}} = 280\ ^\circ\text{C}$ can be calculated to

$$\epsilon = \frac{5.662\text{Å} - 6.126\text{Å}}{6.126\text{Å}} = -7.57\% \tag{4.2}$$

The lattice parameter of GaAs (5.662 Å at $T_{\text{growth}} = 280\ ^\circ\text{C}$) is used here, because the CdSe layer is deposited on fully strained ZnSe layers. For the evaluation of the island density distribution function and the island size distribution function, a series of CdSe QD samples were grown with different CdSe coverage. The CdSe quantum dot samples show typical structural features, which are depicted in figure 4.1. Two different types of islands can clearly be distinguished, large islands indicated by arrows with a diameter of about 16 nm±5 nm (type B-islands), and small islands with diameters below 10 nm (type A-islands). The type A-islands can be identified by a typical small-scale speckle contrast which is clearly visible under weak-beam conditions which is depicted in the inset of figure 4.1.

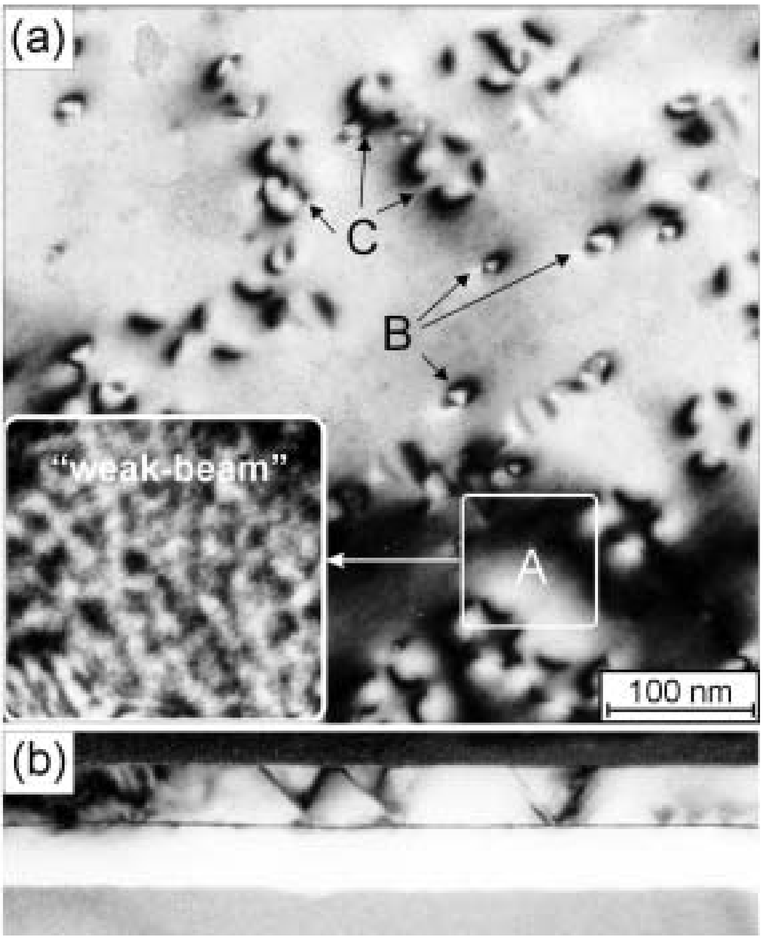

Figure 4.1: TEM plane-view image of a sample consisting of 3.1 MLs CdSe embedded between 45 nm ZnSe. Two different types of islands can clearly be distinguished, large islands indicated by arrows with a diameter of about 16 nm±5 nm (type B-islands), and small islands with diameters below 10 nm (type A-islands). These can be identified by a typical small-scale speckle contrast, which is clearly visible under weak-beam conditions, as shown in the inset of figure a. Figure b shows a dark-field cross section image of the sample [Schi00a, Schi00b].

From the TEM pictures, we get an indication for a bimodal quantum dot morphology. Optical measurements corroborate this assumption. Fig. 4.2 shows the photoluminescence spectrum of a CdSe QD structure under weak excitation conditions.

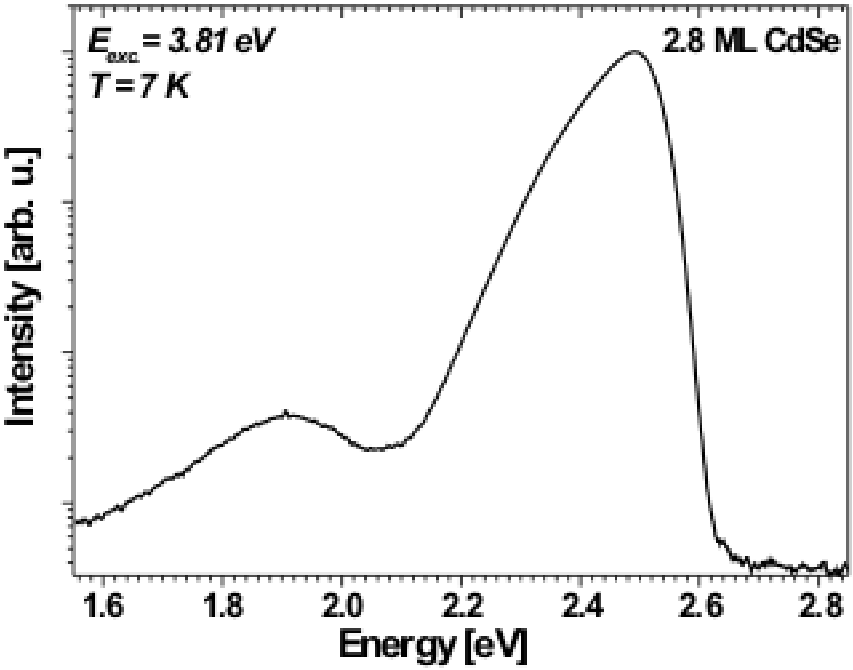

Figure 4.2: Photoluminescence spectrum of a CdSe QD structure under weak excitation conditions. The radiative recombination of excitons localized in QD leads to the broad asymmetric emission at 2.5 eV. The emission at 1.9 eV is caused by deep centers in the ZnSe matrix [Grim77, Grim79].

The radiative recombination of excitons localized in QDs leads to the broad dominating emission at 2.5 eV. The emission at 1.9 eV is caused by deep centers in the ZnSe barrier [Grim77, Grim79]. Due to the bimodal structure of the QD morphology, the emission at 2.5 eV is shaped asymmetric. It will be shown in the following chapters, that type A-islands with densities of 10^{11}cm^{-2} contribute to the high energy side of the emission, whereas type B-islands with densities one order of magnitude lower contribute to the low energy side of the emission. A first confirmation is obtained by cathodoluminescence measurements with high spatial resolution which is shown in figure 4.3.

Depicted are two spectra taken on different sides of the PL spectrum. On the low energy side (green), sharp emission lines dominate the spectrum, whereas on the high

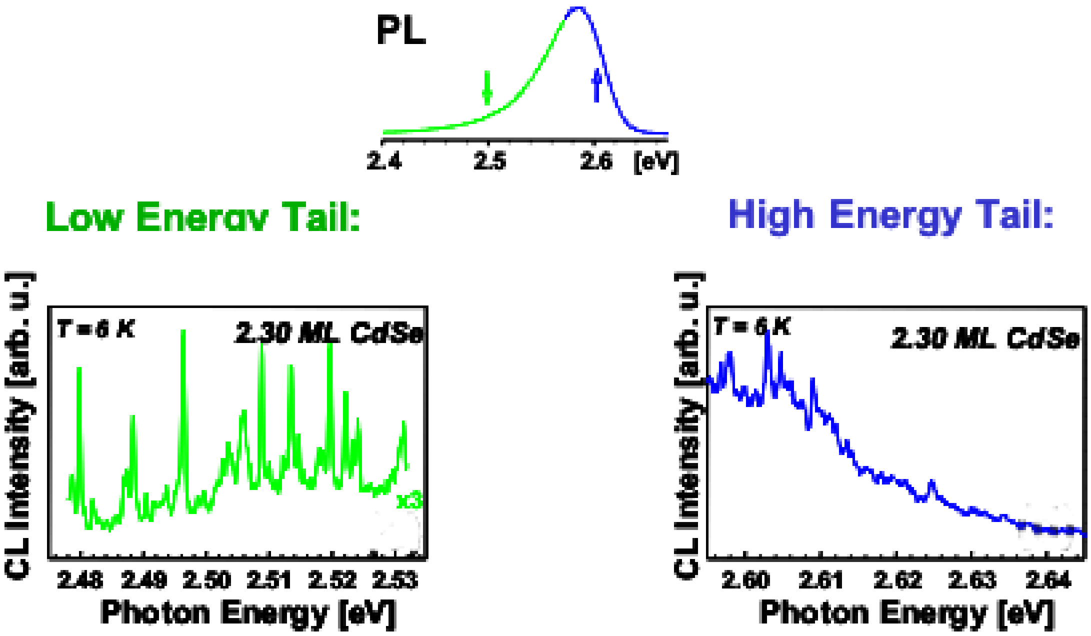

Figure 4.3: Spatially resolved low temperature Cathodoluminescence of CdSe quantum dots. Discrete peaks on the low energy tail (green) are assigned to “large” type B-islands. On the high energy side (blue), single peaks cannot be resolved due to the high density of the type A-islands. The spectrum on top shows the PL of the sample, the arrows indicate the detection positions for the CL [Stra00a].

energy side (blue), single type A-islands cannot be resolved, due to their higher density (see also chapter 4.2.1).

Structural investigations by TEM plane view images (figure 4.1) as well as photoluminescence (figure 4.2) and cathodoluminescence measurements (figure 4.3) reveal a bimodal quantum dot morphology for the system CdSe/ZnSe. The different types of islands are

- small type A-islands with a diameter <10 nm and a density of 10^{11}cm^{-2}
- large type B-islands with a diameter of 16 nm±5 nm and a density of 10^{10}cm^{-2}.

4.1 Formation of type A-islands

The properties of CdSe QD structures, grown by submonolayer deposition of CdSe have been reported several times [Ivan96a, Ivan96b, Lede96, Kres99, Enge99]. These structures are a result of a special deposition procedure and are therefore not comparable with the type A-islands which form self-assembled.

The existence of a bimodal quantum dot morphology is known from the similar system InAs/GaAs [Heit97a]. Since the value of the strain energy in the system GaAs/InAs is nearly equal to the value in the system CdSe/ZnSe, it sounds plausible enough, that these effects occur in the II-VI system too.

To investigate the formation process, series of samples are grown with a coverage of CdSe less than 2.1 MLs to prevent the formation of type B-islands (see also chapter 4.2). The parameters varied are the substrate temperature, the type of the substrate (exact oriented or vicinal tilted) and the growth mode (MBE, ALE or MEE) to find out whether the density of type A-islands depends on the substrate temperature, which would be a sign for a thermodynamically controlled process or depends on kinetic parameters, like substrate-orientation or MBE-process mode. Additionally, annealing experiments are performed to get evidence on the stability of the type A-islands.

The coverage of CdSe is varied between 1.1 MLs and 2.0 MLs, the growth temperature differs from 230 °C up to 340 °C. Each experiment consists of two samples with different types of substrate, one with an exactly oriented GaAs (001) surface, the other one with a 2 ° tilted surface. All samples are investigated by high resolution TEM images.

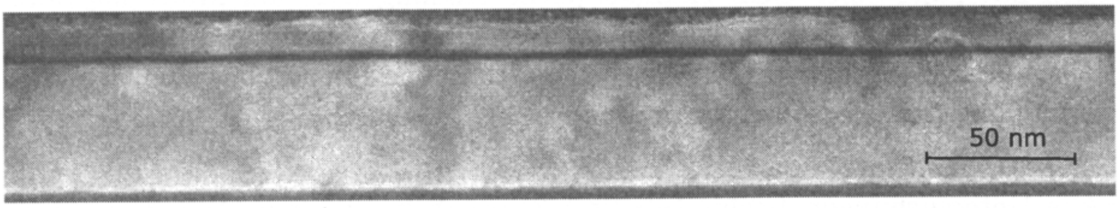

Figure 4.4: The TEM cross section dark field image shows a closed layer of CdSe (2 MLs) buried between ZnSe layers. The image was taken on a (100)-cross section sample.

Figure 4.4 shows a TEM cross section image of a sample with 2 MLs of CdSe buried between ZnSe layers. The CdSe layer is clearly visible as a dark contrast.

The amount of CdSe deposited has a clear influence on the Cd-content of the wetting layer, however the layer is extremely inhomogeneous. An analysis of the Cd-content is possible by means of computer-aided image-processing (CELFA - Composition Evaluation by Lattice Fringe Analysis [Rose98, Rose99]) on high resolution TEM cross section images.

In figure 4.5 color-coded CELFA-analysis on CdSe samples are shown in cross section for different coverage. The layers are also inhomogeneous in lateral direction. Cd-rich inclusions are formed, the fluctuation islands (type A-islands) [Stra98a, Kres98a, Schi00a] are also visible in TEM plan view images.

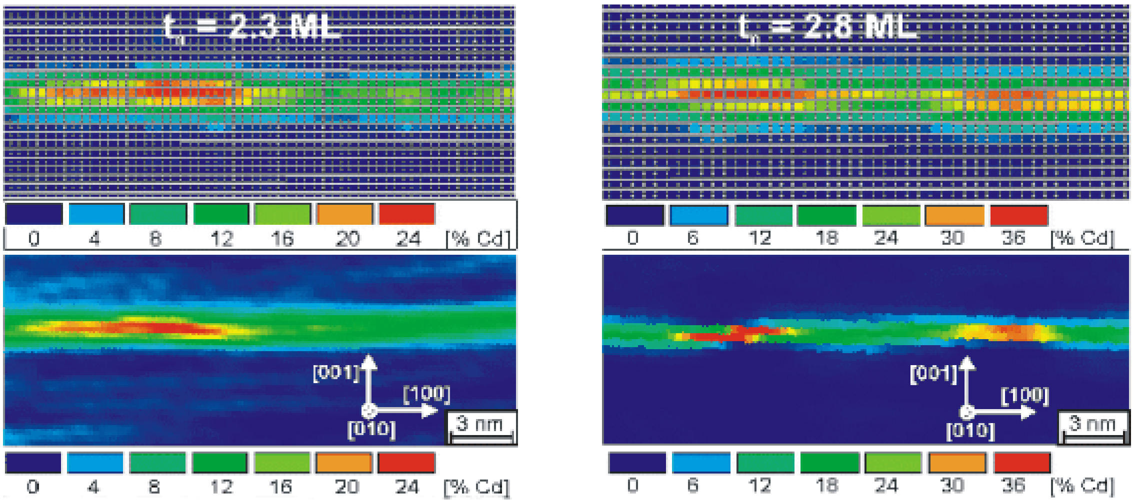

Figure 4.5: CELFA analysis of the Cd-content after deposition of 2.3 MLs and 2.8 MLs CdSe respectively. The structures were capped with a layer of ZnSe [Stra00b].

Figure 4.5 shows (Zn,Cd)Se islands with comparatively high Cd-content, located in the (Zn,Cd)Se wetting layer, represented in green color. The surrounding ZnSe layers are colored blue, whereas small island areas, represented in red color, indicate the type A-islands with a characteristic diameter of 5 nm.

The analysis of these CELFA images reveals:

- The wetting layer is broadening up to nine MLs due to interdiffusion.
- The type A-islands, which appear as Cd-rich inclusions, are embedded in the wetting layer
- The lateral extension of the type A-islands is below 10 nm typically.
- The wetting layer dimension and the island dimension do not significantly depend on the coverage Θ_{CdSe}.

- The Cd concentration in the quantum well and in the islands increases as a function of the coverage (see also figure 4.6).

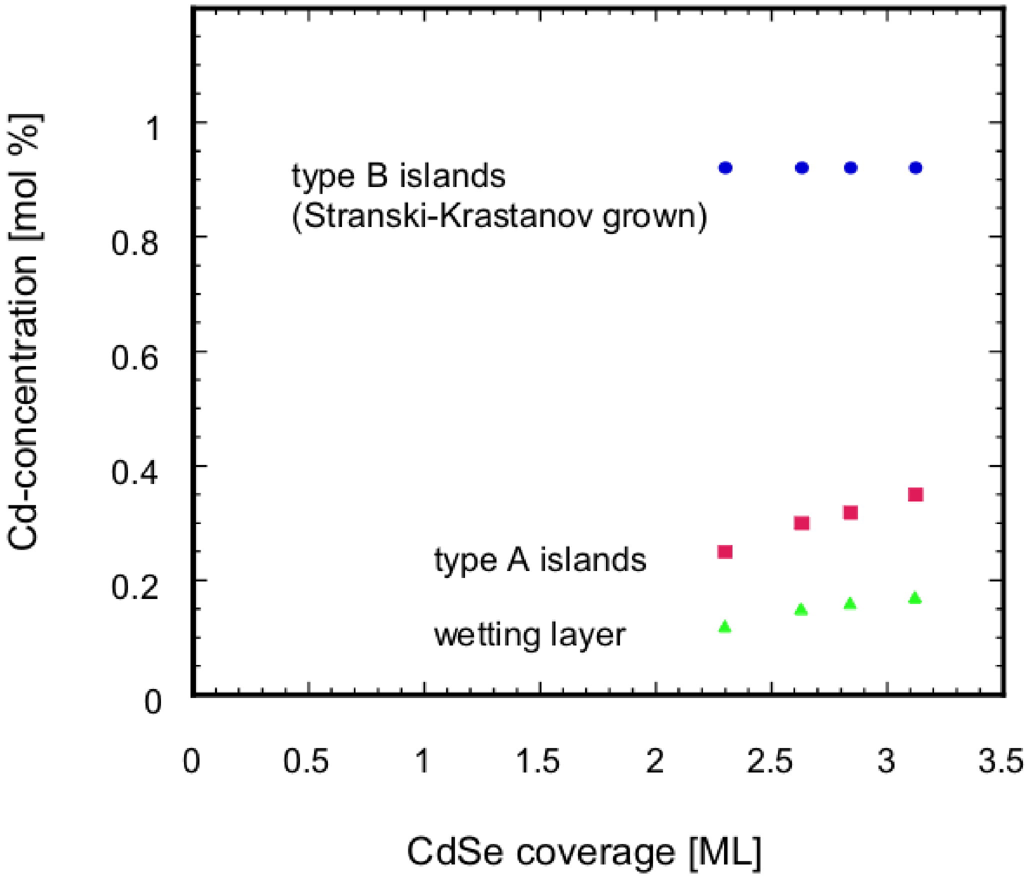

Figure 4.6: Cd content of type A-islands versus the amount of CdSe deposited on samples with bimodal QD ensembles. The Cd content of the type B-islands and of the wetting layer is displayed, too.

Figure 4.6 shows the Cd-content of the type A-islands, the type B-islands and the wetting layer as function of the coverage. With increasing CdSe coverage, the Cd-content of the type A-islands increases, too. This increase is correlated with an increase of the Cd-content of the (Zn,Cd)Se wetting layer. Diffusion is suggested as the driving force, causing the initial two-dimensional two MLs thick CdSe wetting layer turn into a (Zn,Cd)Se compound crystal with a thickness of 2–3 nm. Due to the bandgap of the type A-islands which is smaller than the one of the ZnSe matrix, they are expected to trap excess carriers in shallow localized centers.

The type B-islands, formed by a Stranski-Krastanow growth process, show obviously no dependence on the CdSe coverage. Diffusion processes between these islands and the surrounding ZnSe layers seem to be of minor importance.

To clarify the physical process of the formation of type A-islands, we investigated thermodynamical and kinetic influences of the formation process. CdSe layers with layer thicknesses of 1.1, 1.3, 1.6 and 1.8 MLs were grown at 230 °C and 340 °C respectively and afterwards capped with 45 nm of ZnSe. The density of the type A-islands is investigated by TEM plane view image analysis in "weak beam" mode. A variation of 110 °C absolute in the substrate temperature shows no significant influence on the density. At 230 °C it was found to be $6 \cdot 10^{11}\mathrm{cm}^{-2}$, whereas at 340 °C it was $9 \cdot 10^{11}\mathrm{cm}^{-2}$ in average. There is no difference in the limits of accuracy, the densities are equal.

Variation of the substrate temperature within the range of possible growth temperatures the growth process shows no significant influence on the density of the type A-islands, the formation process seems to be mainly kinetically controlled.

Therefore, in the following experiments parameters were changed, which influence the kinetics of the adatoms and the diffusion velocity on the growing surface. The first case is realized by variation of the substrate type, exact oriented or vicinal tilted by 2° and 6° to the [110] direction respectively. To influence the diffusion velocity, the classic MBE growth mode was compared with migration enhanced epitaxy (MEE). The supply of metal atoms takes place discontinuously and with adjustable incoming frequency. For further details on the growth modes, refer to chapter 3.3. The results are shown schematically in table 4.1.

Table 4.1: Formation of "small" type A-islands.
(+): type A-islands are formed; (−): type A-islands do not form.

parameters	MBE		MEE	
	Se-stabilized	Cd-stabilized	Se-stabilized	Cd-stabilized
0°	+	-	+	-
2°	+	-	+	-
6°	-	-	-	-

The formation of type A-islands can be influenced by variation of kinetic parameters. On substrates with a vicinal tilt of 6°, type A-islands never occurred. Those surfaces consist of steps with a large height and small width, which reduces in general the diffusion length of the adatoms. Another important factor is the stoichiometry of the growth process. At Cd-rich growth conditions, formation of type A-islands is avoided. It is a well known fact, that growing of II-VI semiconductors at Cd-rich conditions increases the surface roughness, which reduces the diffusion length of the adatoms too.

On the other hand type A-islands are always formed at Se-rich growth conditions, i. e. realization of a high diffusion length of the adatoms. Even on substrates tilted by 2°, RHEED oscillations of growing CdSe are measured in nearly all experiments. The diffusion length is obviously higher than the average width of the steps on the surface.

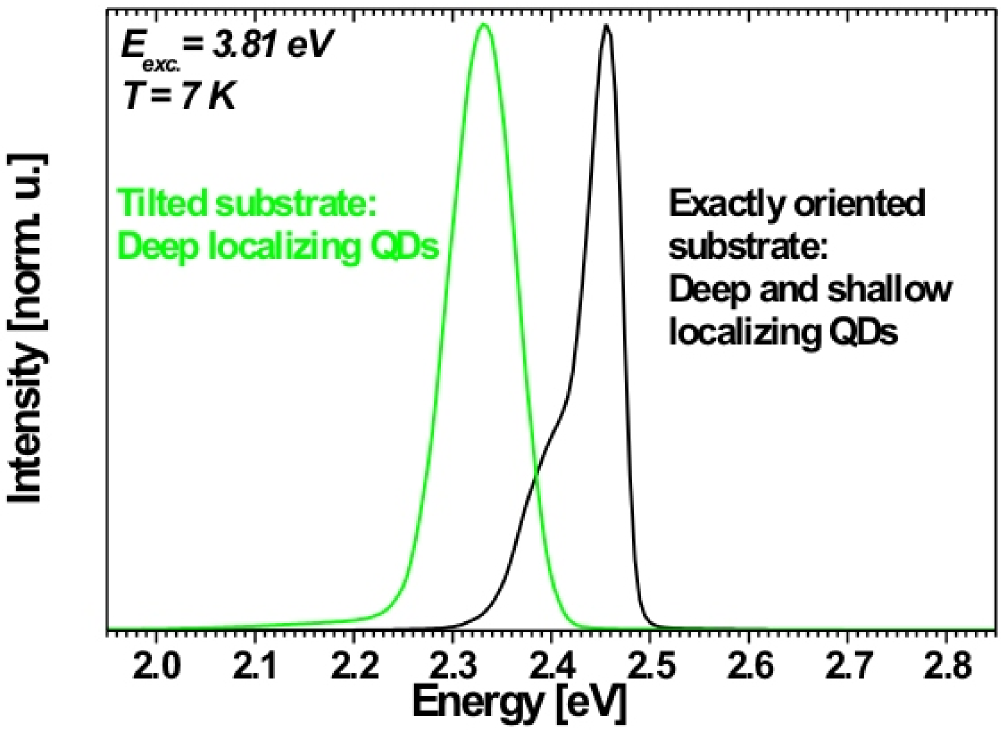

Figure 4.7: Photoluminescence spectrum of a sample with solely deep localized type B-islands (green) compared with a spectrum of a sample with deep and shallow localized type A- and type B-islands (black) [Stra00c].

The suppression of type A-islands can be observed in the photoluminescence spectrum of the according samples. Figure 4.7 shows the luminescence of two samples, which differ only in the orientation of the GaAs-substrate. The spectra also differ in two significant ways:

- The emission energy shifts 125 meV to lower energies on samples on vicinal substrate (6°).
- The emission line changes from an asymmetric shape (sample on exact oriented substrate) to a symmetric shape (sample on vicinal substrate (6°).

The type B-islands are responsible for an emission shoulder on the low energy tail of the emission line, which appears in bimodal quantum dot structures only. We assume that at low temperatures the maximum of the emission peak is dominated by the excitons localized in the type A-islands. The observed asymmetry of the emission line is a characteristic sign for the coexistence of a bimodal quantum dot structure, consisting of different deep localized quantum dots [Stra00a]. On the other hand on tilted substrates (6°), the luminescence is formed only due to excitons recombining in deep localized quantum dots. Without type A-islands the maximum of the emission peak shifts 125 meV to lower energies. The shift is mainly due to the lower ground state energy of the type B-islands as compared to the type A-islands. Small differences in the size and the Cd content of the type A-islands cannot be excluded compared to the type A-islands grown on exact oriented substrates and may contribute to the observed redshift also.

We conclude that formation of type A-islands is favored by the high diffusion length and atomically flat surfaces. However, these conditions are necessary to grow layers in a Frank-van-der-Merwe growth mode, which on the other hand has to be reached for a Stranski-Krastanow process to get a two-dimensional wetting layer.

Figure 4.8 shows a simplified model for the formation of type A-islands. The influence of high elastic strain reduces the lateral growth velocity of the FM-islands continuously, since the strain energy maximum is located at the edges of the islands. It becomes energetically preferable for the adatoms to build a new layer on top of the island, instead at the edges. The higher the cluster grows, the higher the ability to deform and to reduce strain energy.

This model shows the fundamental difficulty to avoid a bimodal size distribution of quantum dots. The Stranski-Krastanow process for the type B-islands requires high elastic strain in a two-dimensional wetting layer, which on the other hand favors the

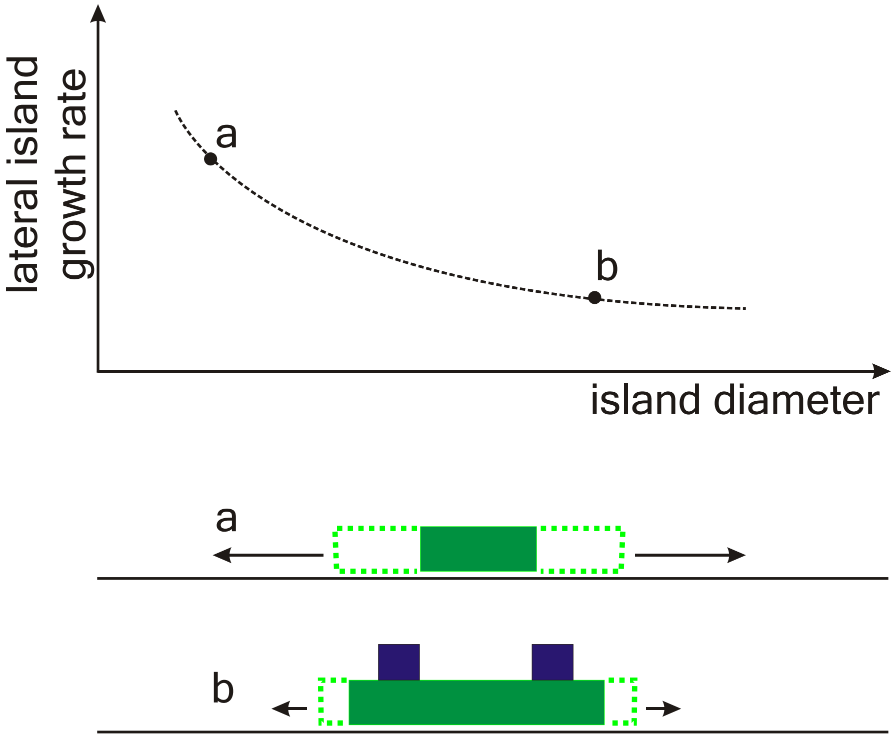

Figure 4.8: Model of type A-island formation influenced by pseudomorphic strain. a) small islands → large growth rate, b) large islands → small growth rate.

formation of type A-islands. The requirement of one process is the driving force of the other one.

On account of the formerly mentioned influence of interdiffusion on the formation of compound crystals in the wetting layer and the type A-islands, annealing experiments are carried out to gather more detailed information. The samples are annealed in an inert gas atmosphere at atmospheric pressure at 230 °C for 48 hours.

As shown in figure 4.9, the Cd-content of the type A-islands increases after annealing. This is a behavior opposite to a normal diffusion regime, where concentration differences are reduced. The gradient increases, the maximum Cd-content in the annealed sample reaches 23%, in the unannealed one 13%.Both samples are grown in the same MBE run, i. e. the deposited amount of CdSe matches exactly in both samples (Θ =1.6 MLs). The annealing is responsible for the observed accumulation of Cd in the type A-islands. The measured changes of the Cd-content can only be explained on the basis of “uphill”-diffusion or spinodal decomposition, respectively [Cahn68, Lang75].

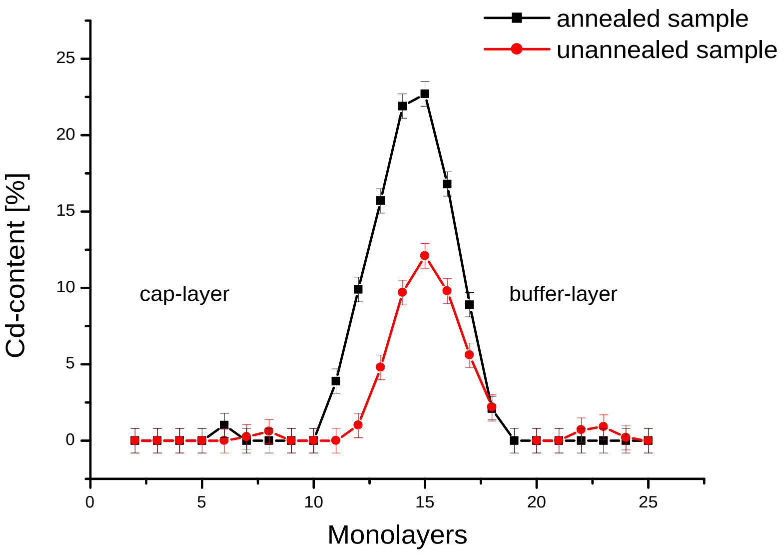

Figure 4.9: Cd-content of type A-islands parallel to the growth direction. Both samples have a deposit of 1.6 MLs of CdSe, the substrate temperature was 230 °C. The red curve shows the Cd-content of the unannealed sample, the black curve shows the Cd-content of the annealed sample (under vacuum conditions for 48 hours at 230 °C) [Schä00].

The analysis of the CELFA images and variation of kinetic and thermodynamic parameters reveals:

- Small QD density and size is not influenced by growth parameters like temperature, coverage or annealing after growth. The formation is not thermodynamically controlled.

- The formation of the small QD could be influenced by growth on vicinal oriented surfaces and is therefore kinetically controlled.

4.2 Formation of “large” islands of CdSe (type B)

4.2.1 Island density distribution function $p_i(\Theta)$

Investigations on the island density distribution took place in cooperation with the University of Karlsruhe, Laboratory of electron microscopy. Therefore, a series of samples with different coverage of CdSe were grown on a 45 nm thick ZnSe buffer layer. The coverage was varied between 0.5–4.5 MLs with an accuracy of ±0.2 ML. The deposited amount was increased in steps of 0.2 ML.

All other parameters were kept constant, i. e. substrate temperature and growth stoichiometry.

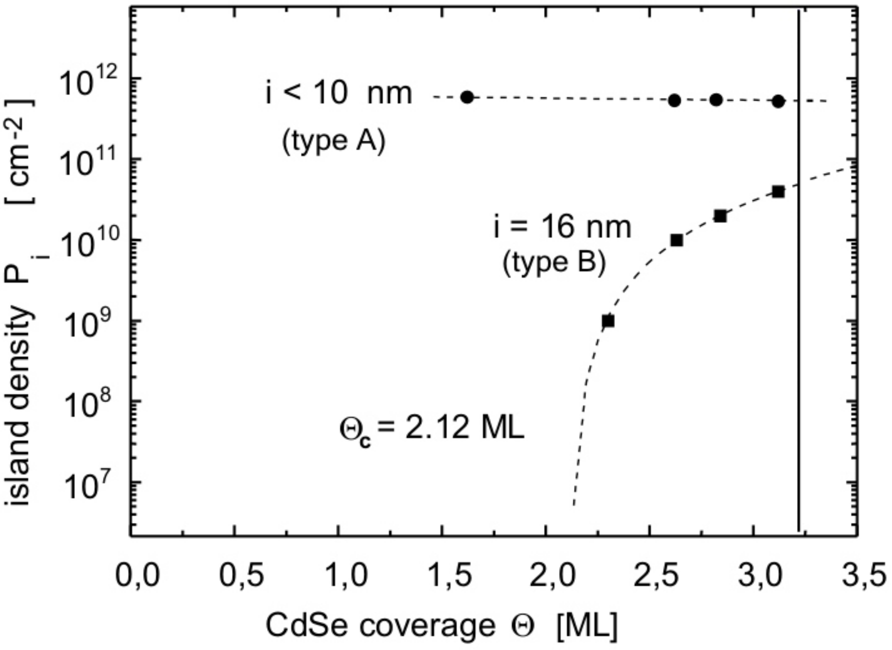

Figure 4.10: Island density distribution function for type A-islands (i<10 nm) and type B-islands (i∼16 nm). The CdSe was deposited on fully strained ZnSe buffer layers with a thickness of 45 nm [Schi00a, Schi00b].

The island density distribution function reveals a super-linear increase of the type B-island density after exceeding a critical threshold coverage Θ_c. Assuming a first order phase transition, the data of the island density distribution function $p_i(\Theta)$ was fitted with a function of the form $p_i(\Theta) = p_0(\Theta - \Theta_c)^{\alpha}$.

With $p_0 = 6 \cdot 10^{10}\text{cm}^{-2}$ and $\alpha = 2.08$ a critical thickness of Θ_c =2.1 MLs was evaluated.

Analogous measurements for the InAs/GaAs system, for the first time reported by Leonard and Petroff from University of California in 1994 [Leon94], a value of $\alpha = 1.8$ for the exponent was found.

An increase of the density by orders of magnitude at a critical thickness Θ_c is a characteristic feature of the Stranski-Krastanow (SK) growth. The analysis revealed, that the type B-islands are formed after reaching a critical thickness (threshold value) of Θ_c =2.1 MLs and have an exponential dependence on the coverage. The type A-island density therefore is independent on the CdSe-coverage.

4.2.2 Island size distribution function $s_i\,(\Theta)$

The analysis of the island size distribution function gives evidence, whether the pseudomorphic strained islands tend to an equilibrium size or if they grow depending on the amount of CdSe deposited.

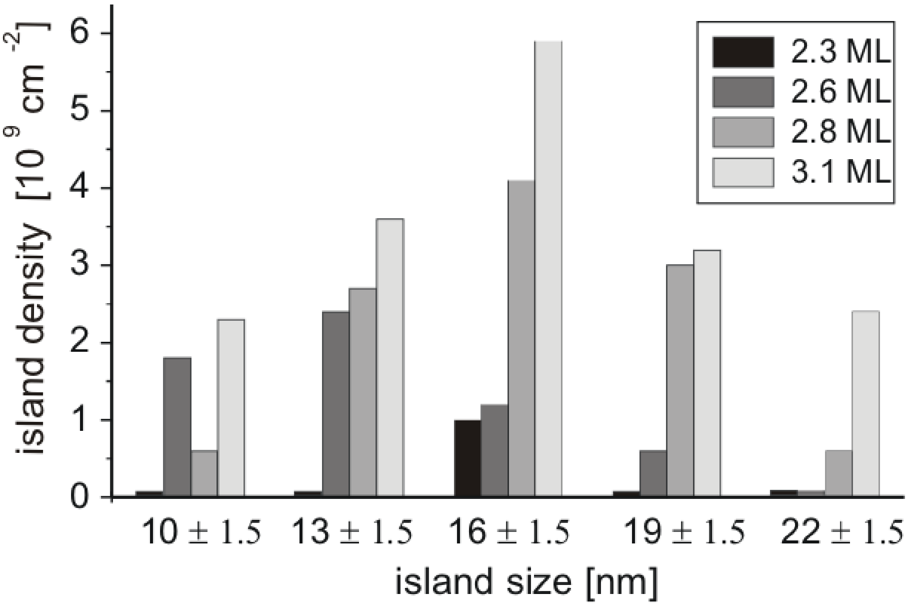

Figure 4.11: Island size distribution of CdSe type B-islands as function of the CdSe-coverage.

Figure 4.11 shows the results of the distribution analysis. The parameter varied is the coverage of CdSe. An important fact is that the type B-islands are capped with ZnSe, that means they are not in the state of as-grown. This has to be taken into account. We assume that the step of overgrowing does not change the size distribution, only the absolute size of the islands. In addition it has been verified that the contrast is caused by CdSe-clusters and not by nearly similar looking stacking faults.

Figure 4.11 shows that the size distribution is independent on the coverage, i. e. the amount of CdSe deposited. A similar behavior was observed for InAs/GaAs SK grown islands, therefore we conclude that the existence of a saturation size of 16 nm in the island distribution is a characteristic feature and typical for the SK growth mechanism. Increasing the excess material on the surface does not result in larger islands but increases the island density, see also fig. 4.10.

Table 4.2 shows a typical series of samples realized by MBE growth for investigations on the island size and density distribution of type B-islands.

Table 4.2: Typical series of samples for the analysis of the island density distribution and the island size distribution. The Cd-content and the island density are evaluated by TEM investigations, layer thickness and CdSe coverage are determined by RHEED oscillations.

sample	CdSe493	CdSe496	CdSe497	CdSe498	CdSe499
ZnSe-Cap (ALE)	45 nm	45 nm	45 nm	45 nm	45 nm
CdSe (MBE)	3.1 ML	2.8 ML	2.6 ML	2.3 ML	1.7 ML
ZnSe (ALE)	45 nm	45 nm	45 nm	45 nm	45 nm
GaAs-substrate	(100)	(100)	(100)	(100)	(100)
density of type B-islands [cm^{-2}]	$5 \cdot 10^{10}$	$2 \cdot 10^{10}$	$1 \cdot 10^{10}$	$1 \cdot 10^{9}$	—

4.2.3 The “growth window” for type B-islands

The analysis of the island density distribution revealed a minimal coverage of Θ =2.1 MLs for the start of the Stranski-Krastanow growth process. The maximum amount of CdSe for fully strained layers was determined by means of RHEED growth oscillations. At a deposition of CdSe above the critical thickness Θ_{crit} plastic relaxation occurs.

Figure 4.12 represents growth oscillations of CdSe on ZnSe at substrate temperatures of 260 °C and 340 °C respectively. The oscillations damp down after the third maxima in both cases due to plastic relaxation. At high substrate temperatures the damping of the

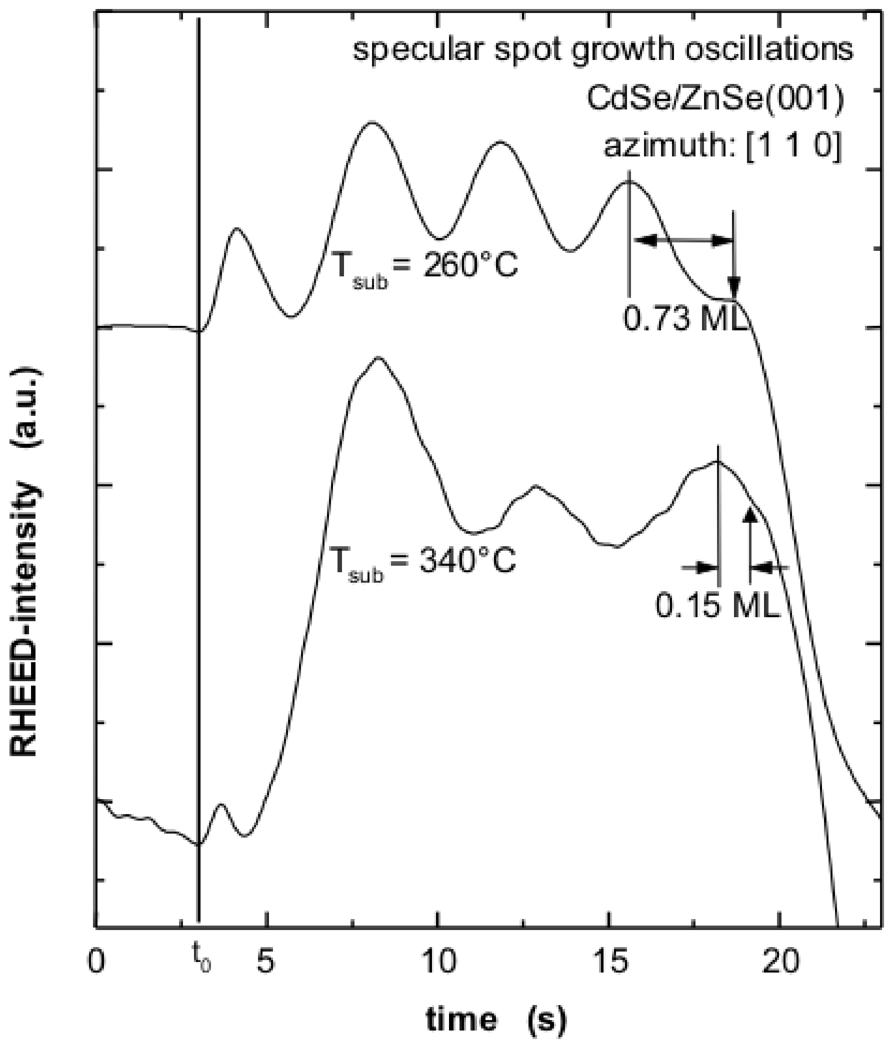

Figure 4.12: RHEED oscillations of the deposition of CdSe on (001) ZnSe at different substrate temperatures. A sharp decrease of the intensity of the specular spot is clearly observable after the deposition of 3 MLs. At higher substrate temperatures the decrease occurs earlier [Schi00b].

oscillation occurs earlier which may be due to the higher mobility of dislocations, which glide to the interface and cause a faster relaxation.

We may draw another conclusion from the damping of the oscillations. In this phase of the growth process there is no significant interdiffusion between the CdSe wetting layer and the ZnSe buffer layer. With increasing substrate temperature the critical layer thickness would increase due to the reduced metric mismatch ϵ, which would be the result of an interdiffusion process.

From the island density distribution function and from CdSe RHEED-oscillations, the growth windows for the type B-island formation is found to be of about 1 ML.

- 2 MLs is the critical threshold coverage for the SK-formation (compare chapter 4.2.1).
- 3 MLs is the critical threshold coverage for plastic relaxation.

4.3 Reversibility of the island formation process

The assumption of a Stranski-Krastanow growth mode for the type B-islands arises from the analysis of the island density distribution function and the island size distribution function. To clarify this, some experiments were performed which took the thermodynamic model of the SK growth mode as a base.

Figure 4.13 shows a phase diagram, published by I.Daruka and A.L.Barabazi [Daru97]. It is based on the reduction of the free energy in a system containing a planar wetting layer with full pseudomorphically strained three-dimensional islands. Displayed are the different growth modes and their areas of existence as function of the coverage H in monolayer and the metric mismatch ϵ.

In the system CdSe/ZnSe the metric mismatch comes to $\epsilon \approx -7.5\%$. A coverage of three monolayers results in a point on the Stranski-Krastanow growth mode marked by a solid arrow in figure 4.13. A condensation of three monolayers CdSe on ZnSe should lead to a formation of three-dimensional CdSe-islands on a CdSe wetting layer, which is confirmed by the experimental data. Reducing the lattice mismatch by a factor of two, the system enters a phase region of a Frank-van-der-Merwe growth mode. A planar and two-dimensional surface would be the energetically most preferred and stable case, in figure 4.13 marked by a dashed arrow.

From these considerations the following model arises: A replacement of all the Se-atoms by S-atoms in the CdSe-islands and the CdSe wetting layer would reduce the lattice mismatch by a factor of more than two. The metric mismatch of the CdS/ZnSe system is about -3.9%. The three-dimensional islands formed at a deposition of three

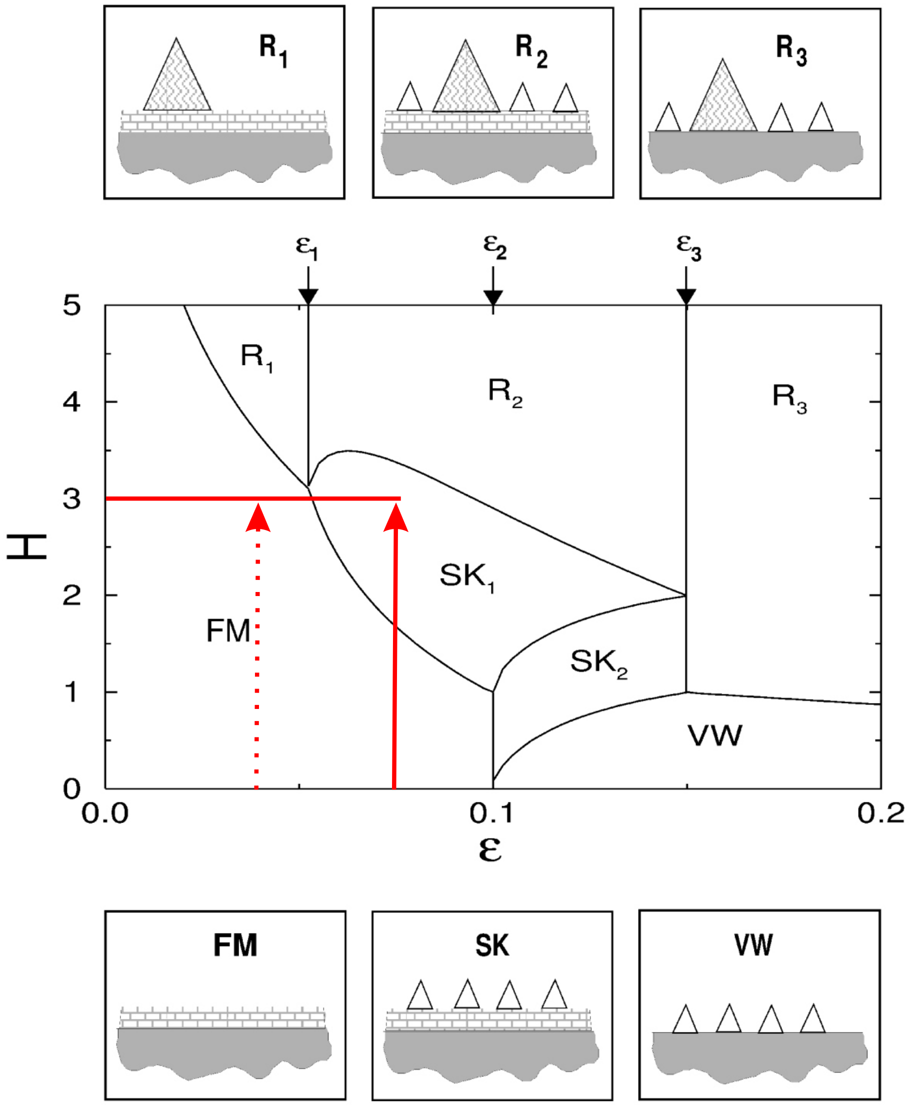

Figure 4.13: Equilibrium phase diagram as function of the coverage H and misfit ϵ. The small figures on top and bottom illustrate the morphology of the surface in the six growth modes. The small empty triangles indicate the presence of stable islands, while the large shaded one refers to ripened islands [Daru97].

monolayers of CdSe should recede, because the Stranski-Krastanow growth mode is no longer the energetically preferred one and the growth region of Stranski-Krastanow is left.

The experiments to prove the reversibility of the formation process of the CdSe type B-islands are carried out in the following way. Three monolayers of CdSe are deposited on a buffer layer of ZnSe, which has a thickness of 45 nm. Three-dimensional CdSe islands are than formed on a planar wetting layer. The phase transition of the surface is monitored by RHEED qualitatively and quantitatively. Figure 4.14 shows a typical RHEED-sequence of the 2D→3D transition.

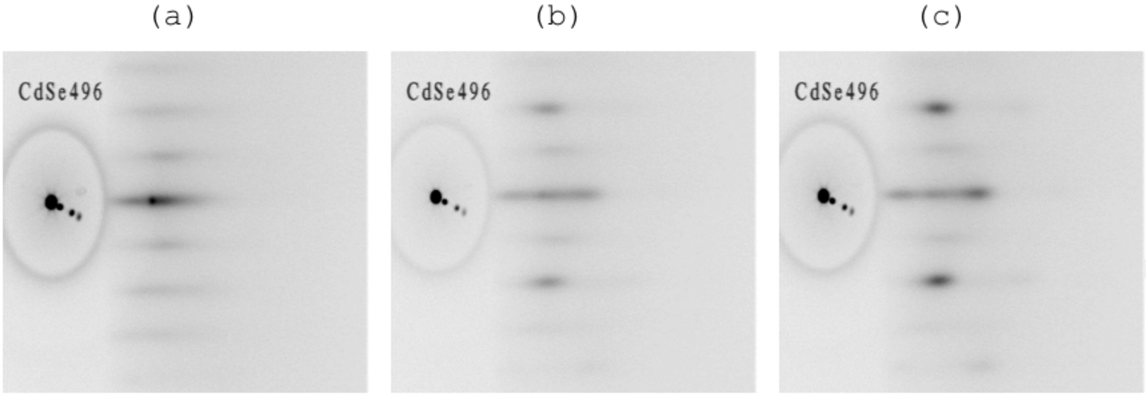

Figure 4.14: RHEED sequence of the phase transition after deposition of 2.8 MLs of CdSe. (a) shows the RHEED pattern directly after deposition of 2.8 MLs of CdSe at a substrate temperature of $T_S = 265°\text{C}$. (b) shows the beginning of the SK-process initialized by an increase of the substrate temperature. (c) shows the superposition of 2D-reflexes from the wetting layer and 3D-reflexes from CdSe islands.

After the formation process the RHEED-pattern looks like a superposition of 2D-surface reflexes, located on Laue-circles, and 3D-transmission diffraction reflexes, not located on Laue-circles. The 3D reflexes are independent on the incident angle of the electron beam, which proves the transmission diffraction origin of these reflections. On the base of the mentioned density of CdSe type B-islands $p = 10^{10}\text{cm}^{-2}$ and a size of 16 nm in diameter and 3–5 nm in height, we calculate a filling factor of 2% of the surface, which explains the RHEED pattern.

After formation, the 3D-islands are normally stabilized under a Se-atmosphere to prevent desorption. Maintaining stationary conditions, the Se-atmosphere is replaced by a S-atmosphere with almost identical partial pressures of $3 \cdot 10^{-7}$ torr.

Due to the higher binding energy of CdS as compared to CdSe, The Se-atoms in the type B-islands and the CdSe wetting layer are replaced by Se-atoms. During the replacement, all metal evaporation cells are closed, so there is no growth in process. The system is minimizing internal energy by reducing the strain throughout S-substitution. All the changes are monitored by RHEED and are shown in figure 4.15.

The rough, three-dimensional surface in figure 4.15c is distinguished by characteristic

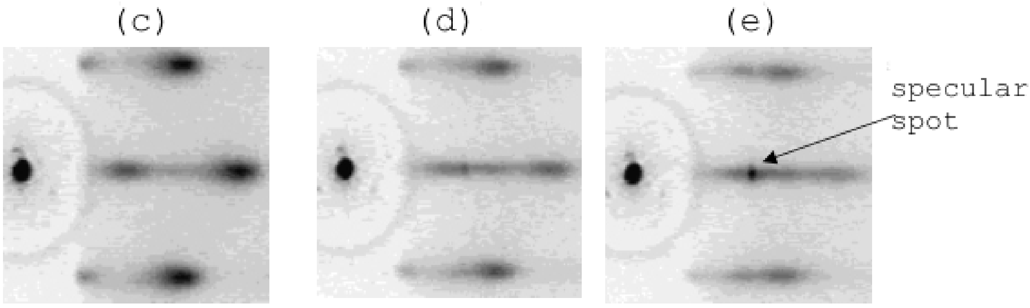

Figure 4.15: RHEED pattern of a CdSe layer after 0 s (c), 40 s (d) and 90 s (e) of exposing to a sulphur atmosphere. The RHEED pattern indicates a transition from a 3D surface to a 2D surface.

3D-diffraction reflexes. The RHEED pattern in 4.15c is similar to the one in figure 4.14c after formation of the 3D-islands. Figure 4.15e shows the reappearing of the specular spot after 90 s of S-exposure time, which is a clear sign for a two-dimensional surface. The 3D-islands have disappeared. Figure 4.15e is nearly identical with figure 4.14a which shows the surface RHEED pattern before the island formation.

The experiments reveal the reversibility of the island formation process of the type B-islands in the CdSe/ZnSe system, which is only possible for thermodynamically controlled phase transitions.

It has been assumed that the reversibility is possible due to the reduction of strain energy in the system CdSe/ZnSe and not due to changes of the chemical potentials on the surface. Additional experiments are performed to prove this assumption. Samples are grown with a CdSe coverage of 3.5 MLs, which is above the critical thickness for relaxation (see also RHEED oscillations in fiture 4.12). The coverage was the only parameter varied. Figure 4.16 shows a comparison between relaxed islands (Θ =3.5 MLs) and fully strained islands (Θ =3 MLs). Whereas the fully strained system reaches a two-dimensional surface after 90 s of sulfur exposure time, the initial relaxed system (at t =0 s) remains three-dimensional. The strain is initially reduced by partial relaxation at the critical thickness. The replacement of selenium by sulphur does not gather enough energy for a phase transition.

The reversibility of the formation process is caused by strain reduction, which is a fundamental characteristic of the Stranski-Krastanow growth mode.

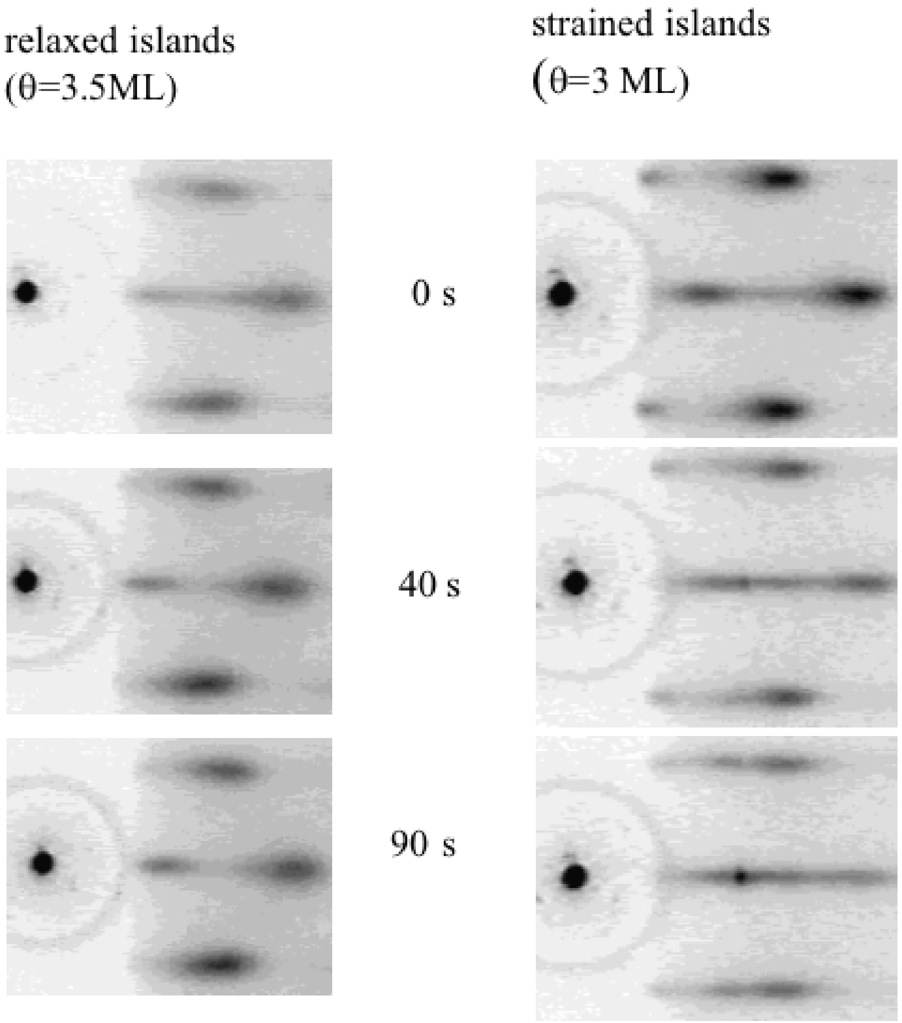

Figure 4.16: Comparison of the behavior of systems with fully strained CdSe SK-islands and relaxed islands, respectively. Both systems were exposed to a stationary sulphur atmosphere. The initial state, that is uncapped SK-islands on the surface of a CdSe wetting layer, is indicated at 0 s exposure time to the sulphur atmosphere [Stra02a].

Table 4.3 lists the experimental data used for the investigations on the 2D→3D phase transition.

The degeneration of the type B-islands is also visible in photoluminescence investigations. Figure 4.17 shows the temperature dependent photoluminescence of a sample with an ensemble of deep and shallow localized quantum dots, i. e. an ensemble of type A- and type B-islands. The matrix-plot is color-coded, bright areas are of high intensity, dark

Table 4.3: Experimental data for the investigations on the reversibility of the phase transition.

sample	CdSe723	CdSe724	CdSe725	CdSe727
ZnSe-Cap	45 nm	45 nm	45 nm	45 nm
sulphur exposition time	0 s	10 s	40 s	90 s
CdSe (MBE)	∼3 MLs			

areas of low intensity. The white lines show the redshift, expected for the ZnSe barrier [ODon97], the energy values on top of the plot indicate the corresponding PL maxima at 5 K and 200 K, respectively. Samples with an ensemble of shallow and deep localized quantum dots always show a much stronger redshift than predicted for the ZnSe barrier.

Up to T=120 K the emission line is dominated by the excitonic recombination in shallow localized quantum dots, the type A-islands. With increasing temperature, the maximum of emission shifts to lower energies, following the shift predicted for the ZnSe bandedge (indicated by the white line in figure 4.17). The shape of the emission line is broadened on the low energy tail due to the contribution of deep localized quantum dots to the photoluminescence.

Above T=120 K a strong redshift (≈170 meV) appears. This is noticeable more than predicted by the redshift of the ZnSe bandedge of ≈60 meV and observable in all samples with deep and shallow localized quantum dots. The shape of the emission line also changes. The intensity of the emission on the low energy side increases, whereas the intensity of the luminescence on the high energy side decreases. The extreme redshift is in contradiction to a static localization in the deep localized quantum dots, because their Cd content and binding energy is high enough to ensure a stable localization of excitons and carriers. However, the density of the type B-islands is too low for tunnelling processes contributing to the observed redshift. Defect luminescence of the ZnSe barrier and the (Zn,Cd)Se quantum well are not observed in this spectral range. Therefore the strong redshift can be attributed to a thermally activated redistribution process. This extreme redshift is typical for samples with an ensemble of shallow **and** deep localized quantum dots.

By exposing the CdSe quantum dots to a stationary sulphur atmosphere, the temperature dependence of the PL signal changes significantly. Figure 4.18 shows another

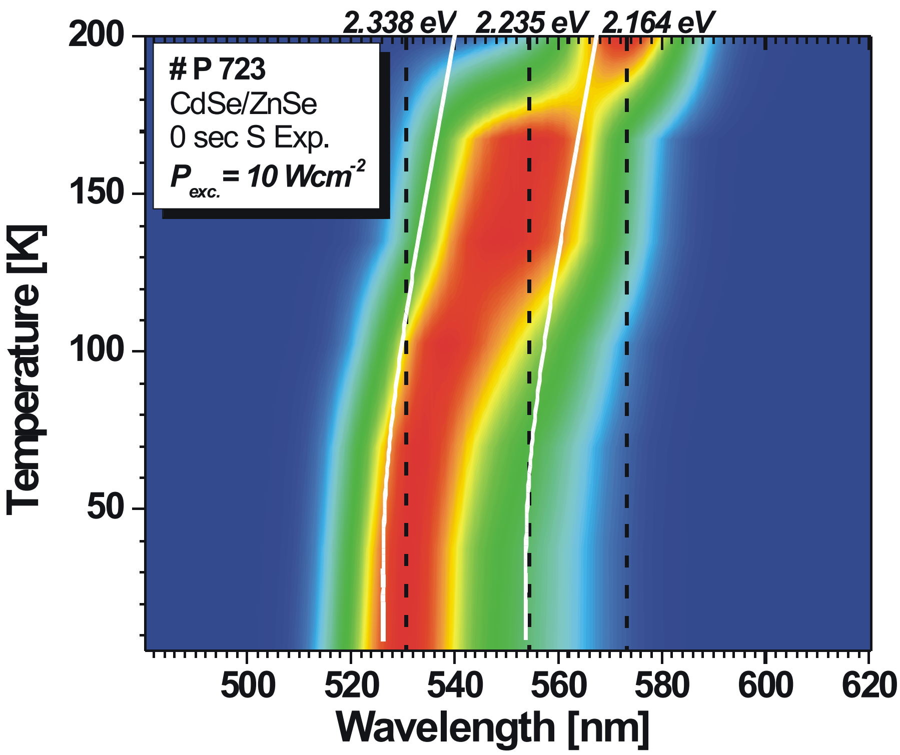

Figure 4.17: Matrixplot of the normalized photoluminescence as function of the temperature for a sample with an ensemble of shallow and deep localized quantum dots. The intensity of the PL signal is color-coded, bright areas are of high intensity, dark are of low intensity. The white lines illustrate the temperature dependence of the ZnSe bandedge. The energy values on top of the plot indicate the corresponding PL maximum at T=5 K and T=200 K [Stra02a].

color-coded matrixplot of the PL intensity for a sample which was exposed for 15 seconds to sulphur. The white line indicates again the redshift predicted for the ZnSe bandedge, the energy values on top of the plot indicate the corresponding PL maxima for T=5 K and T=200 K. With increasing sulphur exposure time, i. e. with increasing degeneration of the type B-islands, decreases the value of the redshift of the PL maximum. At t=15 s the redshift reaches a value of ≈60 meV, the emission of the quantum dot ensemble follows the bandedge behavior of ZnSe. This behavior indicates a reduction of the confinement of the localization centers or a reduction of the type B-quantum dot number and it also indicates an increasing two-dimensional character of the emission centers. The reversibility and,

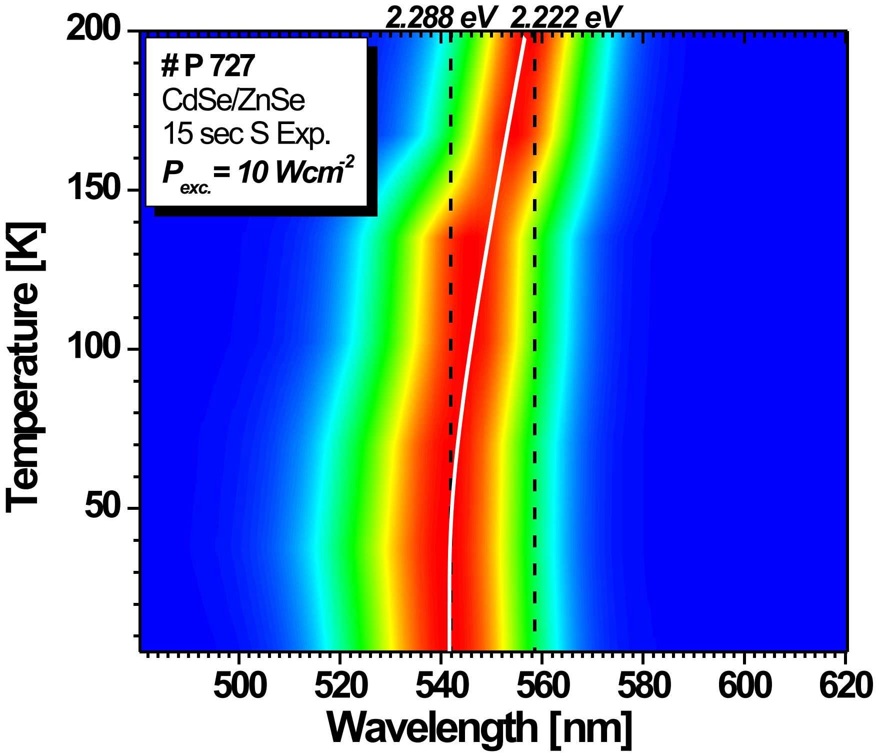

Figure 4.18: Matrixplot of the normalized photoluminescence as function of the temperature for a sample with an ensemble of shallow and deep localized quantum dots after exposing to a sulphur atmosphere for 15 s. The intensity of the PL signal is color-coded, bright areas are of high intensity, dark are of low intensity. The white lines illustrate the temperature dependence of the ZnSe bandedge. The energy values on top of the plot indicate the corresponding PL maximum at T=5 K and T=200 K [Stra02a].

consequently, the thermodynamic character of the type B-island formation is additionally supported by this optical measurements.

The influence of the sulphur exposure caused on the small type A-islands, is not that obvious. The decrease in the halfwidth (Full Width at Half Maximum – FWHM) of the emission line with increasing exposure time is clearly observable and indicates also an influence of the sulphur exposure to the type A-islands.

From optical measurements as well as from the analysis of the island size distribution function and the island density distribution function, we draw the following conclusion.

The large QD are formed by a Stranski-Krastanow growth process with

- characteristic island density distribution function with a nucleation threshold at 2.1 MLs
- coverage-independent existence of a saturation size of 16 nm
- strain controlled reversibility of the SK-formation, which proves the thermodynamic origin.

5 Optical properties of bimodal QD ensembles

5.1 Photoluminescence of bimodal QD structures at low excitation

The luminescence properties of the CdSe quantum dots are investigated by means of photoluminescence (PL) spectroscopy and photoluminescence excitation spectroscopy (PLE). Fig. 5.1 shows the luminescence spectra of samples with different amount of CdSe deposition.

In the spectra a broad asymmetric peak at E≈2.5 eV is dominating. This emission line results from a superposition of radiative recombination of shallow (type A: activation energy E_A =18 meV [Stra02c], temperature dependent photoluminescence) and deep (type B: activation energy E_A =88 meV [Stra02c], temperature dependent photoluminescence) localized excitons. The quantum dots with shallow localized excitons (type A) mostly dominate the luminescence on the high energy side, whereas deep localized excitons (type B) dominate the luminescence on the low energy side of the spectrum. Resolving single dot emission lines is avoided by the high density of quantum dots (10^{11}cm^{-2} and 10^{10}cm^{-2}) respectively, compare chapters 4.1 and 4.2. As seen in Fig. 4.10 the density of type B-islands increases with increasing CdSe coverage, but never exceeds a value bigger than 5% of the density of type A-islands [Schi00a]. The generated carriers are trapped efficiently in the quantum dots, proved by the absence of luminescence originated in the ZnSe-matrix, which is expected at 2.8 eV (for the bandedge luminescence and the excitonic luminescence) and 2.7 eV (DAP luminescence), respectively.

Two additional significant features are observable.

- With increasing CdSe coverage the peak emission of the spectrum shifts to lower

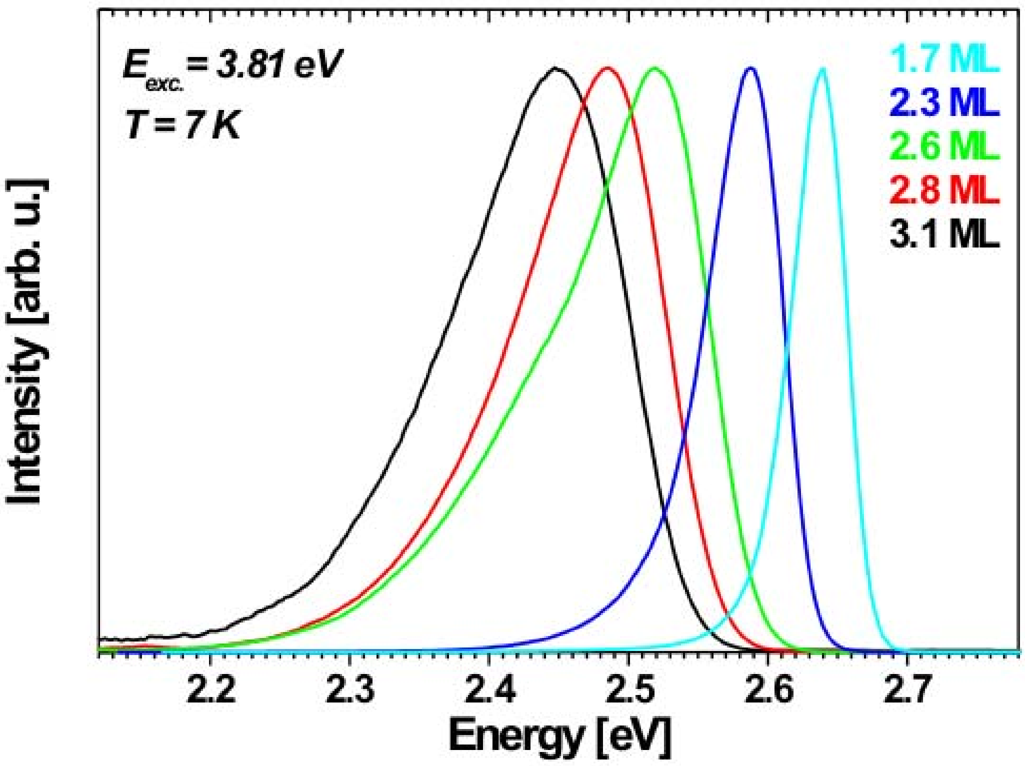

Figure 5.1: Photoluminescence spectra of bimodal quantum dot structures at low excitation. The broad spectral lineshape is caused by recombination of excitons in shallow and deep localized quantum dots. The maximum of the PL luminescence shifts to lower energies with increasing CdSe deposition and the FWHM increases. [Stra00b].

energies.

- The halfwidth (FWHM)of the emission line increases from 45 meV at Θ =1.7 MLs CdSe (only type A-islands) to 145 meV at Θ =3.1 MLs CdSe.

In chapter 4.2, we show that investigations from TEM images reveal no influence of the CdSe coverage on the size distribution of the type B-islands. For a Stranski-Krastanow growth mode the energetic positions of the emission line and the halfwidth should be equal for all samples containing type B-islands.

To clarify the physical reasons for the redshift and the increasing FWHM with increasing CdSe coverage, temperature dependent PL and time resolved PL have been measured.

5.2 Temperature dependent Photoluminescence

A detailed evaluation of the temperature dependent continuous wave (cw) photoluminescence measurements gives evidence over existing redistribution processes between the different quantum dot classes. Figure 5.2 shows the position of the emission maximum and the attached halfwidth (FWHM) as a function of the temperature.

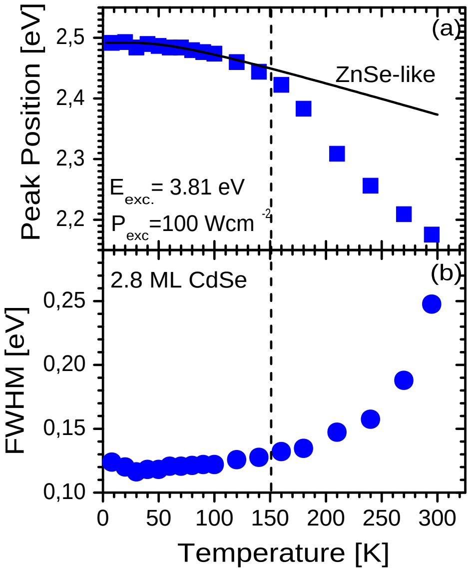

Figure 5.2: Typical temperature dependence of the emission energy of the PL maximum (a) and the halfwidth (FWHM) of the emission line (b) of an ensemble with shallow and deep localized quantum dots. The solid line shows the temperature dependence of the ZnSe band gap. The sample consisted of 2.8 MLs CdSe and was excited at E_{exc} =3.81 eV with an excitation density of P_{exc} =100 Wcm^{-2} [Stra02b].

With increasing temperature the halfwidth as well as the redshift of the emission maximum increases, which is a typical behavior of inhomogeneous quantum dot ensembles with distinct redistribution processes of carriers and excitons [Lobo99].

Depending on the value of the redshift, two temperature ranges can be distinguished. Below T=150 K the redshift follows the one of the ZnSe bandedge and the halfwidth

(FWHM) remains nearly constant. Above T=150 K the redshift and the halfwidth increase clearly. At low temperatures most of the carriers and excitons recombine in shallow localized quantum dots. A small redshift and nearly constant halfwidth with increasing temperature are characteristic features of those quantum dot ensembles. A significant transfer of excitons and carries into deep localized quantum dots does not occur. Above T=150 K the thermal energy kT is of the same order as the binding energies of the shallow localized quantum dots. The mobility of the excitons and carriers increases and the transfer to deep localized quantum dots with lower transition energy increases too. The emission line broadens and the redshift increases. Defect luminescence of the ZnSe barrier and the (Zn,Cd)Se quantum well are not observed in this spectral range. Therefore the strong redshift can be attributed to a thermally activated redistribution process.

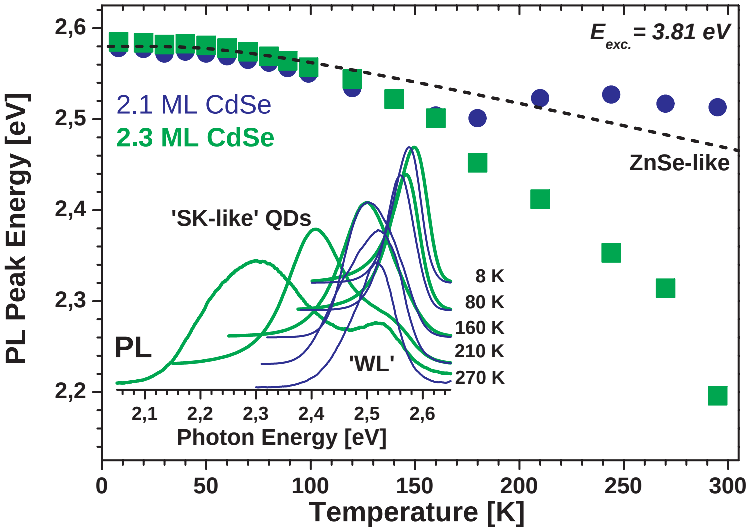

Figure 5.3: Temperature dependence of the photoluminescence maximum for samples with different CdSe deposition. The temperature dependent behavior of the ZnSe bandedge [ODon97] at T=0 K was fit to the emission energy of the quantum dot ensemble. The inset shows PL spectra at selected temperatures, whereas the emission band of deep localized quantum dots is referred as "SK-like" and of shallow localized quantum dots as "WL" [Stra00b].

Investigations on samples with different CdSe coverage reveal that the redshift is typical for samples with shallow and deep localized quantum dots. Figure 5.3 shows the energetic position of the emission maximum in dependence of the temperature for two samples with different CdSe coverage. The inlet shows the photoluminescence spectra at selected temperatures.

In figure 5.3 at low temperatures the luminescence of the two samples with 2.1 MLs of CdSe (only shallow localized quantum dots) and 2.3 MLs of CdSe (shallow and deep localized quantum dots) show similar behavior, because the emission line is dominated by the excitonic recombination in shallow localized quantum dots. The shape of the emission line is also similar, broadened on the low energy tail of the sample with deep localized quantum dots, due to their luminescence contribution.

Above T=150 K the luminescence of both samples shows significant differences. With increasing temperature the intensity of the emission on the low energy tail decreases in the sample without deep localized quantum dots. The halfwidth of the emission line reduces. The maximum of emission shifts to higher energies. At room temperature it reaches a value, which is expected for a two-dimensional (Zn,Cd)Se wetting layer. The blueshift of the emission maximum is a clear sign for a thermal activation of the electrons from the shallow localized quantum dots in an energetic higher state, which is given by the two-dimensional quantum well. The emission maximum follows the shift of the ZnSe bandedge like that of an exciton localized in a quantum well [Bimb99].

Temperature dependent PL spectroscopy reveals:

- Up to T=150 K the PL luminescence is dominated by the recombination of excitons in type A-islands.
- A thermally activated redistribution process takes place for the excitons for samples with an ensemble of shallow and deep localized quantum dots at temperatures above T=150 K.
- For samples with type A-islands only, a thermal activation of the excitons from the shallow localized quantum dots into the ZnCdSe quantum well (wetting layer) occurs at temperatures exceeding T=150 K.

At low temperatures the PL luminescence is dominated by recombination of excitons in type A-islands. With increasing CdSe coverage, the Cd content of these islands increases (see also figure 4.6), which alters the transition energy and leads to the observed redshift of the PL line.

5.3 Photoluminescence excitation spectroscopy (PLE)

The influence of the wetting layer and the Cd content on the observed redshift in the photoluminescence is investigated by photoluminescence excitation spectroscopy (PLE).

In PL measurements, the excitation energy is kept constant. The PL intensity is plotted as function of the detection energy. In PLE measurements, the detection energy is kept constant. The PL intensity at this certain detection energy is plotted as function of the excitation energy.

Fig. 5.4 shows two PLE spectra with different detection energies and the photoluminescence (PL). The detection positions are marked by arrows on the emission line, chosen in a way to detect mainly quantum dots with shallow localization, i. e. detection on the high energy side or with deep localization, i. e. detection on the low energy side. In both cases, excitation above the ZnSe bandedge gives an efficient excitation mechanism. Excitons and carriers generated in the ZnSe matrix recombine in shallow and deep localized QDs.

To understand the excitation mechanism of the different QD classes, excitation below the ZnSe bandedge is of higher interest because the QDs cannot trap carriers and excitons from the ZnSe layers.

For the deep localized quantum dots a broad unstructured band is detected with an increase of the PLE signal at an excitation 28 meV resonantly above the detection energy. This phenomenon is described as phonon assisted absorption. The broad band is caused by population of the deep localized quantum dots through the inhomogeneous (Zn,Cd)Se quantum well. The inset in fig. 5.4 shows the redshift of the photoluminescence maximum and the quantum well luminescence with increasing CdSe coverage. This shows the dominant influence of the average Cd content of the quantum well in contrast to the lateral size of the type A-islands.

For a detection energy on the high energy side, the excitation behavior changes significantly. The formerly broad unstructured emission band shows now distinct equidistant maxima and minima. The difference between two excitation maxima is 31 meV, which

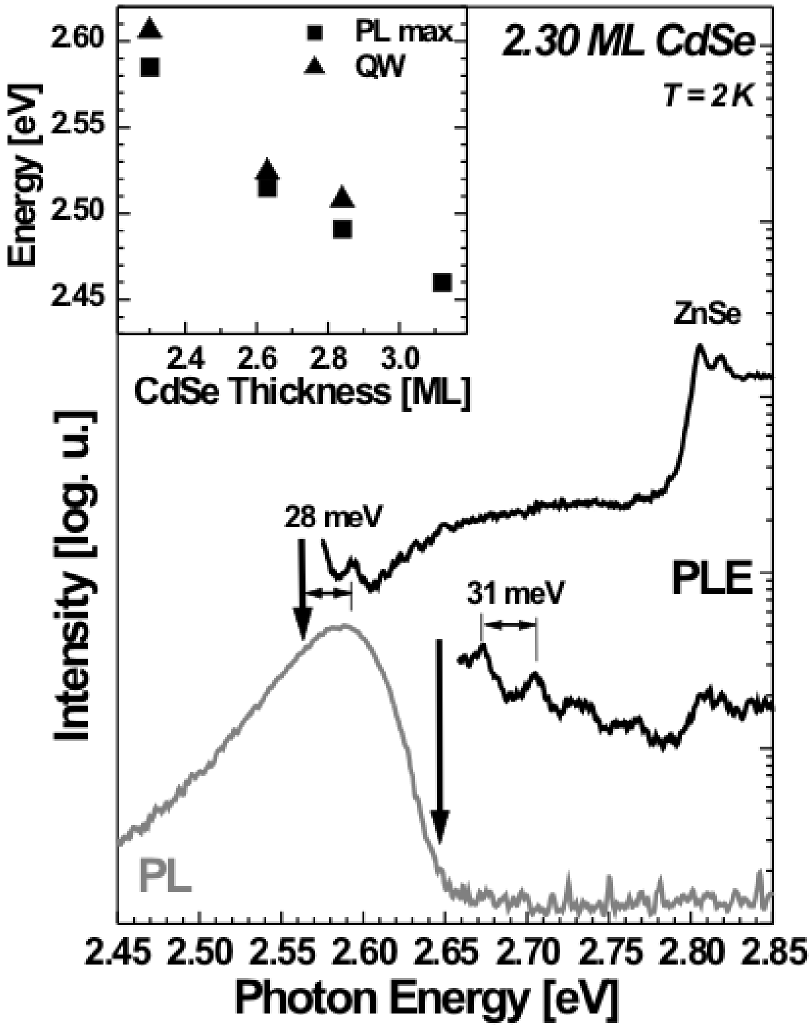

Figure 5.4: Photoluminescence (PL) and photoluminescence excitation spectroscopy (PLE) of a sample with an ensemble of deep and shallow localized quantum dots. The detection energies are marked by arrows on the PL. The inset shows the redshift of the photoluminescence maximum and the quantum well luminescence with increasing CdSe coverage [Stra00b].

is in the range of a LO-phonon in ZnSe or (Zn,Cd)Se with less than 5% of Cd content respectively. This "hot-exciton-relaxation“ is not expected for quantum dots, because it is a property of bulk crystals, whereas quantum dots have discrete densities of state. However, the type A-islands have a very high density. The average space between two neighboring quantum dots is of the same size like the dot itself (≈5 nm). For a "hot" carrier it is nearly always possible to be trapped in a quantum dot with matching ground state energy, accompanied with an interaction of the phonons in the ZnSe matrix. The shallow localized quantum dots have a quasi two-dimensional density of states.

On the other hand the excitation behavior of the deep localized quantum dots differs significantly. Population of states does not take place via neighboring quantum dots, however the shallow localized quantum dots represent an efficient excitation mechanism.

PLE spectroscopy on samples with deep and shallow localized quantum dots reveals:

- Excitation above the ZnSe bandedge is a high excitation mechanism for shallow and deep localized QDs.
- Type B-islands are populated through the inhomogeneous (Zn,Cd)Se quantum well and through shallow localized quantum dots.
- "Hot-exciton-relaxation" reveals the quasi-two-dimensional density of states for type A-islands.

With increasing CdSe coverage increases the density of type B-islands (see also figure 4.10). PLE measurements reveal that population of these islands takes place through the (Zn,Cd)Se quantum well and through the type A-islands. With increasing CdSe coverage the contribution of the type B-islands to the observed PL increases too. In combination with the redshift of the PL maximum with increasing coverage, this leads to a broadening of the PL line and therefore to an increase of the FWHM.

5.4 Timeresolved PL of CdSe QD

A quantitative description of the decay behavior of the luminescence of QDs requires the determination of the radiative lifetime, the transfer time and an average localization energy. These parameters consider radiative (luminescence) and non-radiative (transfer) processes, which involve relaxation of carriers and excitons.

Gourdon and Lavallard [Gour89] proposed a model based on lateral redistribution processes of carriers and excitons. The PL decay time as function of the detection energy is given by:

$$\tau\left(\mathrm{E}\right) = \frac{\tau_{\mathrm{rad}}}{1+\exp\left(\frac{\mathrm{E}-\mathrm{E_{me}}}{\mathrm{E_0}}\right)} \tag{5.1}$$

τ_{rad} is the radiative lifetime, i. e. the time excitons localized in QDs need to recombine radiative.

$\mathrm{E_{me}}$ is the energy, at which the radiative lifetime is equal to the transfertime. At energies higher than $\mathrm{E_{me}}$, non-radiative relaxation into QDs with lower transition energy is more probable than radiative relaxation.

The transfer time is the average time, a carrier or exciton needs to redistribute non-radiative into another QD.

$\mathrm{E_0}$ is the average binding energy, i. e. redistribution processes reach typically final states which are lower by the value of $\mathrm{E_0}$. The average binding energy is a measure for the broadening of so called “tail states”, which are free final states of transfer processes.

Figure 5.5 shows the photoluminescence at continuous wave excitation and the dependence of the decay constant on the detection energy for two different samples at T=7 K and T=160 K. The first sample has been exposed to a sulphur atmosphere (figures a) and b)), before capping with a ZnSe layer. The second one was capped directly after the formation of the type B-islands (figures c) and d)).

At low temperatures, the decay times of the luminescence of the two investigated samples behave similar. We conclude that the sulphur exposition does not suppress the formation of fluctuation islands (type A) completely.

At T=160 K a significant difference is observable. The decay time of the luminescence of the QW-like sample (figure 5.5b) reaches a maximum value of ∼900 ps. This is three times larger than in the QD structures.

Figure 5.6 shows the radiative lifetime as function of the temperature for three samples with different sulphur exposure time (0 s, 10 s and 15 s).

The existence of deep localized QDs is of decisive importance for the radiative lifetime. The type B-islands haven’t completely receded in the samples with 0 s and 10 s sulphur exposure time. Temperature dependent cw PL investigations (see also chapter 5.2) show the existence of deep localized QDs, which enables the three-dimensional confinement of excitons at higher temperatures. Therefore the radiative lifetime shows no dependence on the temperature which is characteristic for QDs [Bimb99].

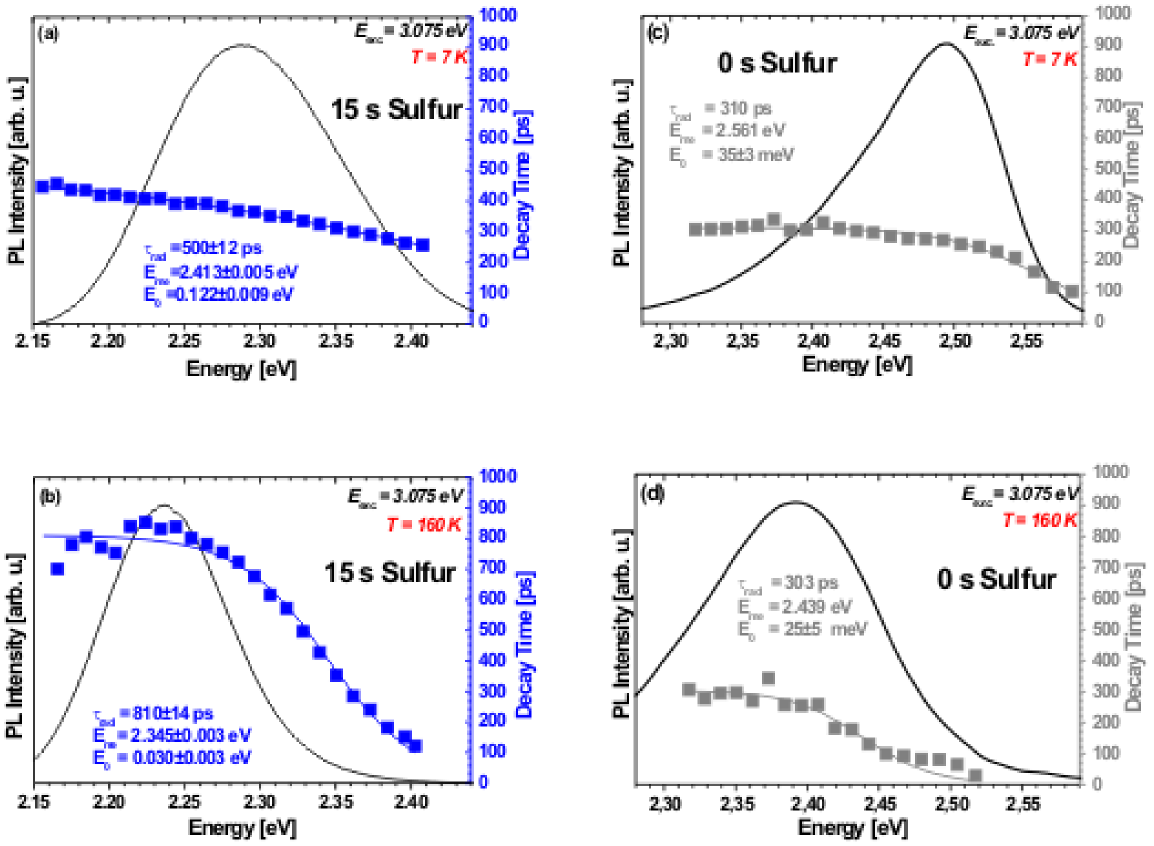

Figure 5.5: Time resolved photoluminescence for two samples with 0 s (c,d) and 15 s (a,b) of sulphur exposition at temperatures T=7 K and T=160 K. The lines represent the photoluminescence spectrum, the squares show the decay time at different energetic positions [Stra02b].

The radiative lifetime of the luminescence of the sample with 15 s sulphur exposure time shows a QW-like characteristic. Above T=100 K τ_{rad} increases linear with the temperature [Feld87]. This behavior is typical for the transition from a zero-dimensional to two-dimensional density of states of the emission centers and has been reported for other materials [Chic01]. With increasing temperature the mobility of excitons and carriers increases which results in a higher spatial separation of electrons and holes. The wave functions separate, the overlap integral decreases and the transition probability decreases. The radiative lifetime τ_{rad} increases.

Figure 5.7 shows the decay times for selected transition energies of a sample with

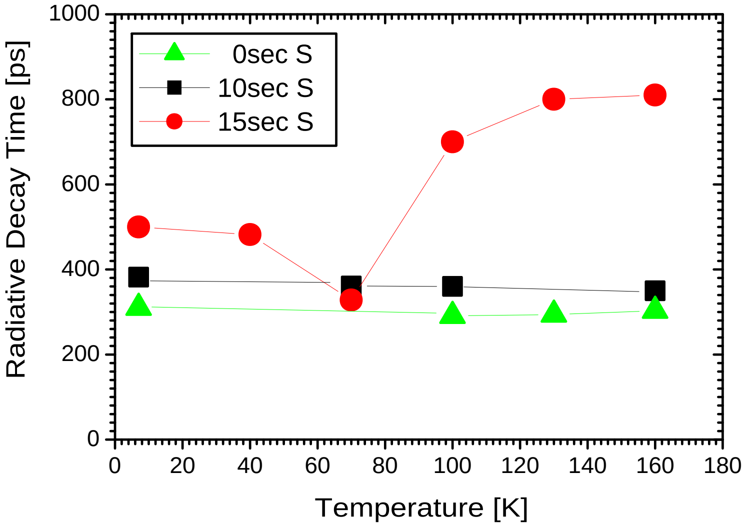

Figure 5.6: Radiative lifetime as function of the temperature for samples with different sulfur exposition time.

2.8 MLs of CdSe coverage at temperatures between T=2 K and T=210 K. The decay behavior of the luminescence of the shallow localized quantum dots gives a distinct hint on the thermally induced delocalization of the excitons. The binding energy of the excitons is typically ∼10 meV, i. e. the excitons loose their zero-dimensional character above T=100 K.

For the carrier and excitons, other processes have to be considered which do not contribute to the emission in the examined energy interval. Due to the thermal induced delocalization, carriers and excitons can faster reach nonradiative recombination sites, and can be trapped in deeper localized quantum dots. These processes are normally faster than the direct radiative recombination of the excitons and dominate the observed lifetime. The temperature dependence of the decay time of excitons in deep localized quantum dots is more stable. The localization of excitons in the quantum dots remains stable at temperatures up to T=210 K, which results in a mainly radiative recombination of the excitons. In this case the decay time should be stable or increase slightly with increasing photoluminescence intensities, which is observable. Due to the bimodal quantum dot ensemble, other processes are involved, which alter the decay behavior. The divergent

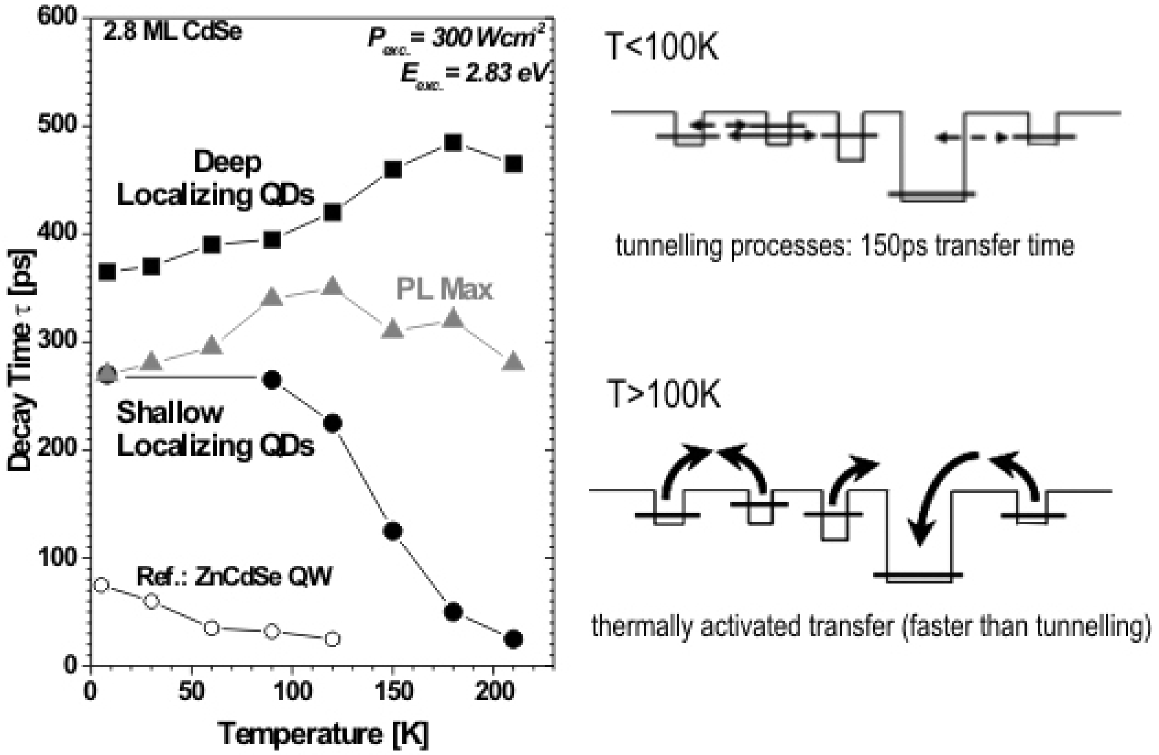

Figure 5.7: Temperature dependence of the decay constant of a sample with 2.8 MLs of CdSe. The detection energies were chosen to detect the behavior of the PL maximum and the behavior of the deep and shallow localized quantum dots. For comparison purpose the decay behavior of a ZnCdSe quantum well with similar emission energy is displayed, too.

behavior is caused by capturing of delocalized excitons and at high temperatures by a thermally induced escape of carriers and excitons out of the deep localized quantum dots.

The summary of the time resolved PL reveals:

- The optical properties of the bimodal quantum dot structures are influenced more by transfer processes than by the size and density distribution of the quantum dots.
- Below T=100 K tunnelling processes are dominating the carrier redistribution, the optical spectra are influenced mainly by the recombination of excitons in type A-islands.
- Above T=100 K thermally activated transfer of carriers from type A-islands to type

B-islands is dominating. The optical spectra are mainly influenced by the properties of deep localized quantum dots.

- The radiative lifetime of type B-islands is about 300 ps and independent on the temperature.

6 Quantum dot spectroscopy

Despite the fabrication of laser structures on the base of CdSe quantum dots as active layer material, other optoelectronic devices such as single photon sources are of great interest. Compared with other single photon emitters, selforganized QD display some important assets. They can be pumped electrically and they can be integrated in high-quality semiconductor microcavities to achieve a single mode behavior and a high photon collection efficiency.

Triggered single photon emission from InAs/GaAs QD has been reported by several groups, but only at temperatures up to T=50 K. To generate single photons from a single QD under nonresonant pumping, it is necessary to filter spectrally the exciton line or one of the multiexciton lines. Due to the small magnitude of the exciton-biexciton splitting for InAs QD (∼1–2 meV) and due to the temperature induced broadening of these lines, spectral filtering cannot be achieved at temperatures T>100 K. In contrast, the II-VI QD show a much stronger Coulomb binding energy, which results in a higher exciton-biexciton splitting (∼20 meV for CdSe) [Gind99b, Kula99]. Therefore such QD structures are very attractive for single photon generation at high temperatures, which has been shown experimentally [Seba02].

Optical investigations in chapter 5 revealed that the small islands (type A) dominate the optical properties at low temperatures. Due to their high density ($5 \cdot 10^{11}\text{cm}^{-2}$) it is very difficult to achieve single dot emission by detecting the PL through a mask with 170 nm apertures [Lee00]. This is also the case for scanning near-feal optical microscopy with comparable resolutions [Flac96]. It would require the fabrication of masks or structures of dimensions of several tens of nanometers, which makes such devices unpractical.

An approach to overcome the high density is to use the inhomogeneity of the density distribution on the sample. This is achieved by using vicinal tilted substrates for the growth process. The distribution of QDs will be localized in the vicinity of the steps. With increasing distance to the steps the density decreases. Apertures of 500 nm are sufficient to achieve single QD spectroscopy using micro-photoluminescence (μ-PL). These apertures are made by electron beam lithography and aluminium mask deposition.

Figure 6.1 shows μ-PL spectra of a 2 MLs CdSe QD sample, sandwiched between 45 nm ZnSe layers at T=8.8 K, detected with apertures of sizes 10 μm and 500 nm at an excitation density of ≈60 W/cm^2.

Exciting PL over a large area (aperture diameter of L_x =10 μm) of the sample results in an inhomogeneously broadened spectrum with a halfwidth (FWHM) of ≈65 meV. Spike-like structures superimposed on the broad PL band correspond to emissions from QDs, suggesting a rather low QD density distribution. This is confirmed by the μ-PL with an aperture of L_x =500 nm. Single sharp lines appear in the spectrum, which indicate a single QD spectroscopy regime. With increasing temperature these lines merge into the broad PL band and are quenched at T≈115 K, due to the thermal activation of carriers out of the QDs. The broad PL band itself appears up to room temperature.

Assuming that the five lines X_1 to X_5 originate from different QDs, a local QD density of $2 \cdot 10^9$cm^{-2} is evaluated, which is one to two orders of magnitude lower than reported for CdSe samples grown on exact oriented substrates (type A-density ≈ 10^{11}cm^{-2}).

An expanded view with higher resolution of the spectrum of the tilted sample is shown in figure 6.2. The exciton PL line X_5 is accompanied by a broad background (marked by a "◯"), mainly appearing on the low energy side. This broad band is formed by acoustic-phonon sidebands. The FWHM of the zero-phonon line X_5 with a value of 320 μeV is significantly larger than estimated from radiative lifetime recombination. Hundt et al. [Hund01] reported a FWHM of 70 μeV. Investigations with shorter integration time (a few seconds only) showed that the QD emission energy randomly shifted by an amount of the order of 200 μeV, which explains the measured FWHM by using longer integration times. This temporal shift of the emission energy can be assigned to the Stark effect caused by fluctuation of local electric fields [Seuf00]. On the other hand, even if the local density of type A-islands far away from the substrate steps is as low as 10^9cm^{-2}, the aperture size is significantly larger than the stepwidth, i. e. in μ-PL an average density of 10^{10}cm^{-2} is observed. So the number of QDs, illuminated by the laser is in the range of 10–100. Real single quantum dot spectroscopy is not performed, always a group of several QDs contribute to the spectrum.

Figure 6.3 shows the evolution of the exciton lines as function of the excitation density, normalized to the X_4-line. With increasing excitation density, some new lines appear

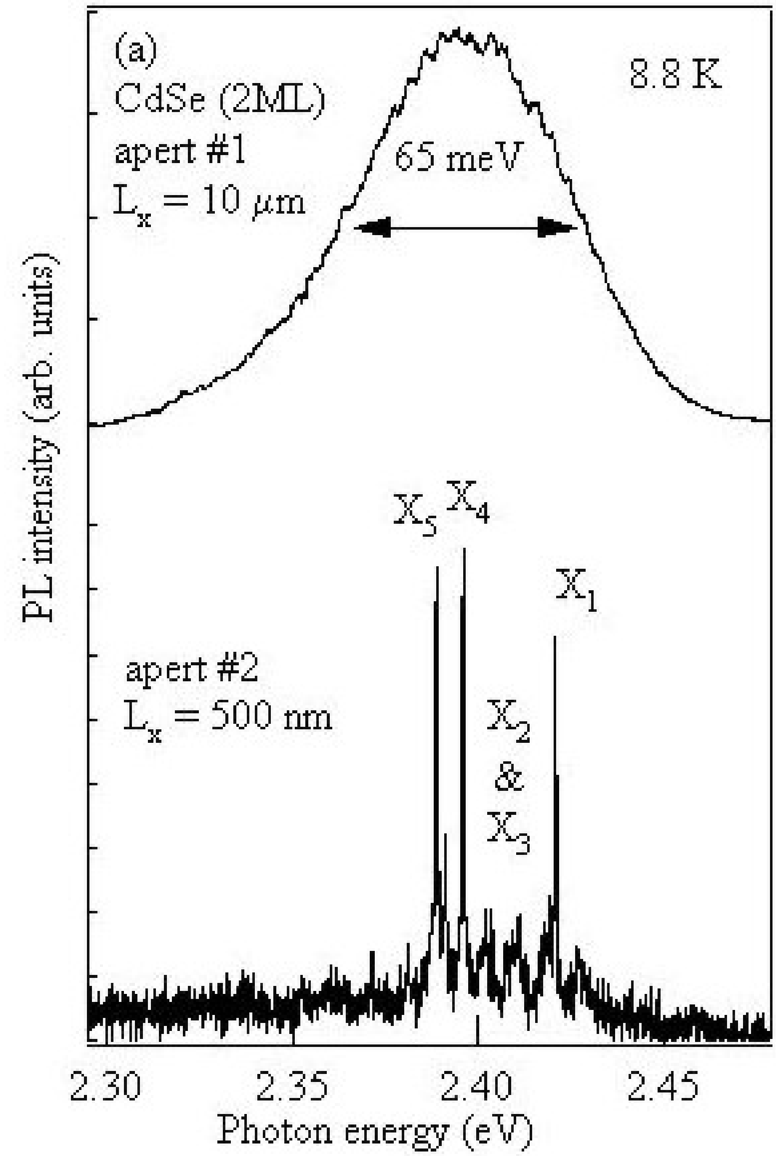

Figure 6.1: μ-PL spectra at T=8.8 K of a type A-island sample (2 MLs of CdSe sandwiched between 45 nm ZnSe layers), grown by MBE on a vicinal GaAs substrate, detected for the aperture sizes L_x =10 μm and 500 nm and an excitation power of $\approx$60 W/cm^2 [Maki03].

(XX_1, XX_4), whereas some lines show a linear or sublinear behavior (X_1, X_4, X_5), other show a superlinear behavior (marked by a "•"). No clear correlation with the excitation density could be established in order to assign a set of lines to a single QD. The sublinear dependence of the lines X_1, X_4 and X_5 on the excitation density suggests a high excitation

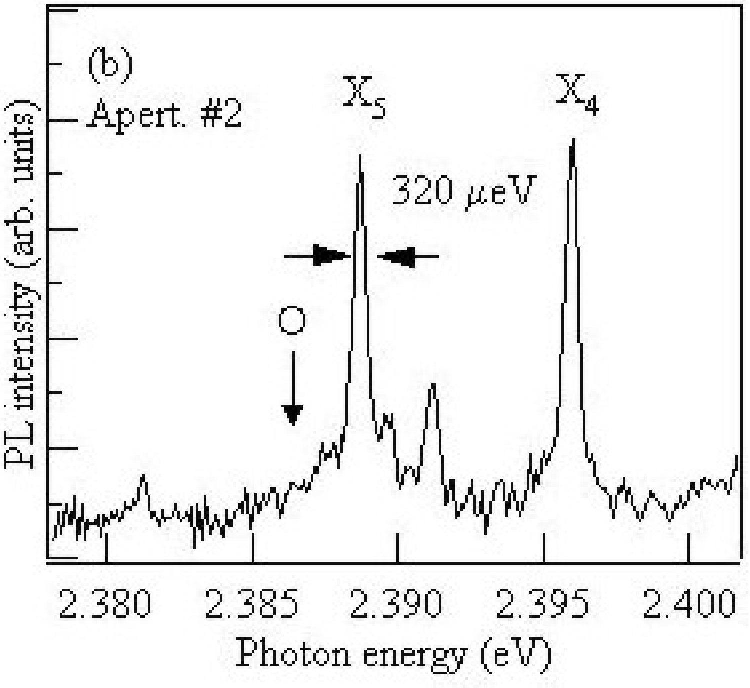

Figure 6.2: Expanded view of the μ-PL of the sample with 2 MLs of CdSe on vicinal tilted GaAs substrate at T=8.8 K detected for the aperture size L_x =500 nm. The open circle represents coupled exciton-acoustic phonon sidebands of the excitonic zero-phonon line X_5 [Maki03].

regime, where QD are occupied by several excitons. Therefore the lines X_1, X_4 and X_5 could correspond to the recombination of excitons and multiexcitons from the same QD, which implies a density $< 10^9 \text{cm}^{-2}$. It has to be noted, that the biexciton binding energy for CdSe/ZnSe QD can be as high as 24 meV, which is about the energy separation between X_1 and X_4.

In summary, investigation on vicinal tilted substrates with CdSe QD layers, which contain only type A-islands, show a local island density $\leq 10^9 \text{cm}^{-2}$, which theoretically allows an observation of single QD spectroscopy for spatial resolutions of 500 nm. Due to an averaging over a still “large” sample area, the number of observed quantum dots is in the range of a few tens to hundreds. The exciton lines are inhomogeneously broadened to 320 μeV, which is most probably due to this excitation of a group of type A-islands.

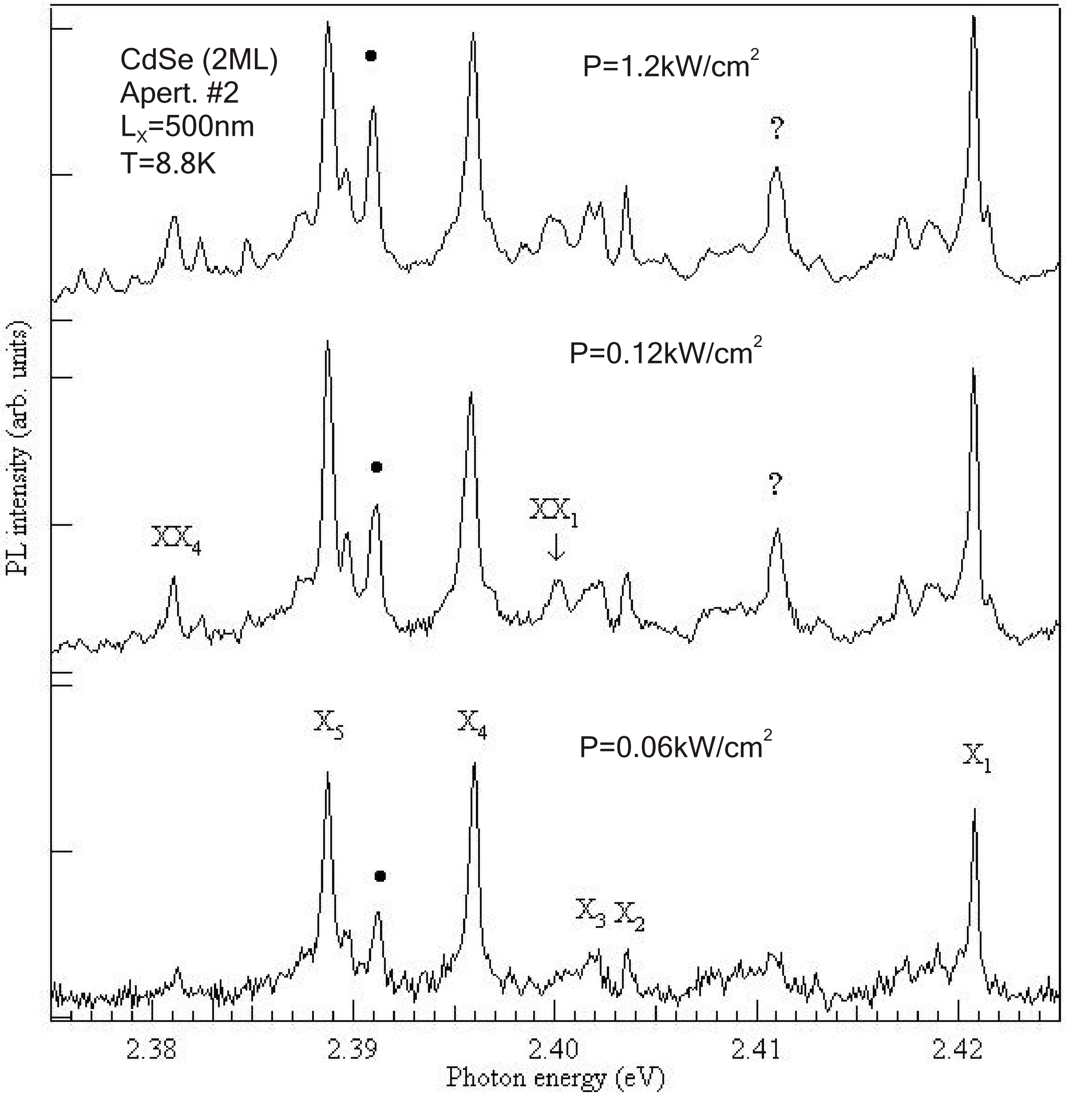

Figure 6.3: μ-PL spectra at T=8.8 K detected for the aperture size L_x =500 nm for various laser excitation powers. The maximum excitation density is 1.2 kW/cm^2. All PL lines are normalized to the X_4 line [Maki03].

7 Stimulated emission and optical gain

In order to fabricate a laser diode with active CdSe quantum dot layers, structures are grown, which show optical gain and stimulated emission. For that, one single CdSe QD layer is not sufficient, therefore ten-fold-stacks were grown.

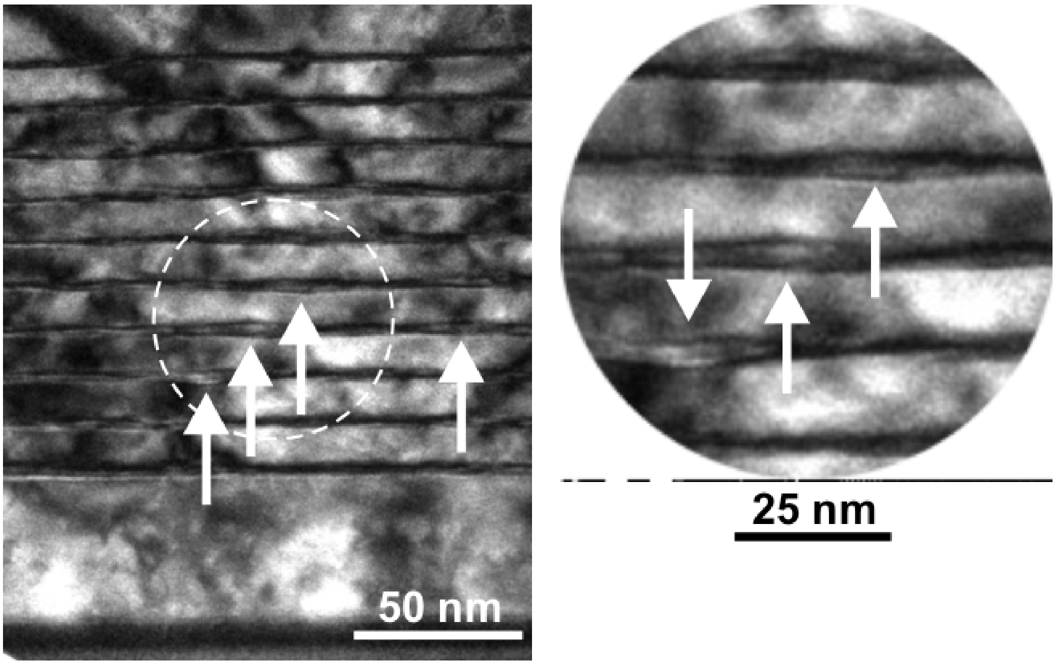

Figure 7.1: TEM cross section image of a ten fold stack of CdSe QD layers grown on a tilted substrate. The type B-islands are indicated by the bright contrast inside the ZnCdSe layer and some are marked by arrows. The inset shows some islands on a larger scale [Stra00c].

Figure 7.1 shows a cross-section TEM image of such a structure with stacked CdSe type B-islands, grown on a vicinal tilted GaAs-substrate [Stra00c]. A relative large number of these type B-islands are revealed by regions with a bright contrast inside the islands, which indicates a high Cd concentration which was estimated to ≥70%. The islands with lateral dimensions around 16 nm in average are embedded in a ~3 nm thick wetting layer with remarkable lower Cd concentration. The height of the islands exceeds that of the wetting layer only slightly. In some places, the island arrangement is laterally shifted in adjacent layers, which occurs particularly in samples on tilted substrates. This behavior is attributed to a preferential nucleation at growth surface steps induced by stacking faults, whose density is increased in the tilted samples. Such an alignment effect of the islands at stacking faults was also found in ZnSe/ZnMgSSe structures [Lüers99].

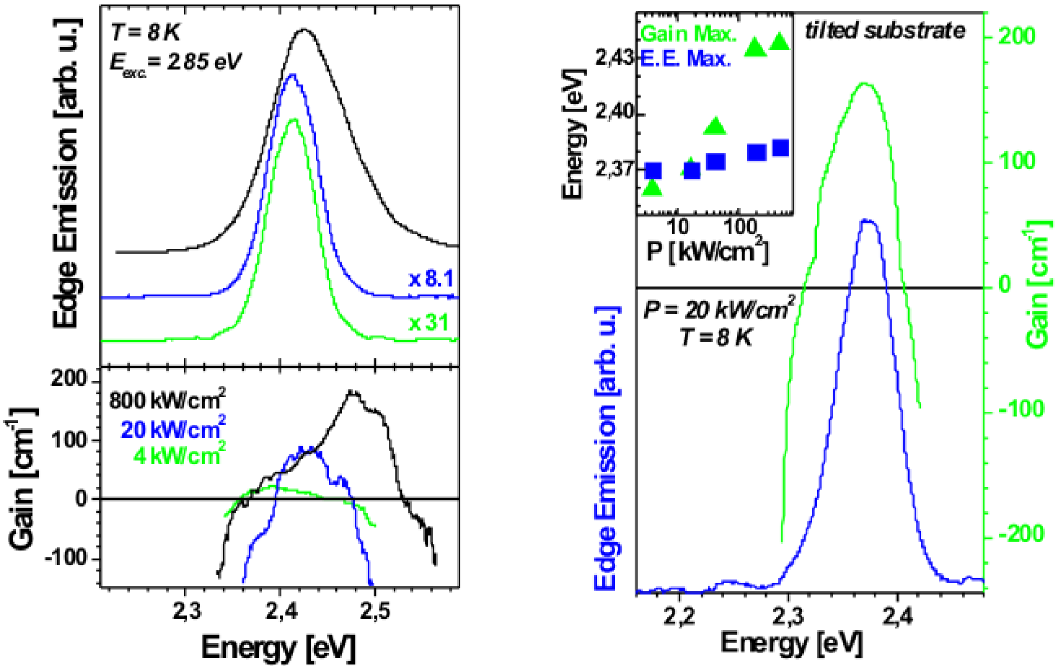

Figure 7.2: Comparison of edge emission and gain spectrum for samples grown on exactly oriented GaAs-substrate (on the left hand) and on tilted substrates with 6° off (on the right hand). On tilted substrates higher gain values are reached (compare lines for 20 kW/cm^2 for example). The inset on the right hand shows the excitation density dependent energy position of the edge emission and the gain maximum [Stra00c].

Figure 7.2 shows the excitation density dependence of the edge emission and the optical gain for samples on exactly oriented and on tilted (6° off) substrates. The samples consist of a ten-fold-stack of CdSe QD (2.8 MLs), separated by 12 nm ZnSe barriers.

With increasing excitation density the edge emission of the sample on the exactly oriented substrate shows no significant change in shape and position of the maximum of the emission band. This behavior is known from recombination of three-dimensionally confined excitons [Bimb99]. These excitons are localized in type A- and type B-islands providing the 3D confinement which is necessary for the radiative recombination of excitons at high excitation energies. At very high excitation densities (800 kW/cm^2), the high energy tail of the edge emission becomes broader and a blueshift of the emission maximum occurs. According to the applied excitation densities this observed behavior is attributed to an increasing population of higher states, e. g. of smaller type A-islands and into the wetting layer. This explanation is supported by the results of gain investigations.

Whereas at the threshold, the gain maximum is observed on the low energy tail of the edge emission, the maximum of the gain shifts with increasing excitation density into the resonant edge emission. Further increase of the excitation density leads to a saturation of the resonant gain at $\sim$40 cm^{-1} and to a strong blueshift of the gain maximum, which is far more pronounced than that observed for the edge emission. This can be attributed to the limited number of islands and to the population of higher states.

The right hand side of figure 7.2 depicts edge emission and gain at an excitation density above the threshold density for a sample grown on a tilted substrate. Gain in resonance to the ground state transition of the edge emission is detected. A further increase of the excitation density leads to a saturation of the resonant gain. In comparison to the sample on an exact oriented substrate, higher gain values are observed, which could be a hint to higher island densities or higher oscillator strength for the localized excitons. Additionally, with increasing excitation densities a broadening of the high energy tail of the edge emission is detected. Simultaneously, an additional feature appears in the gain spectrum on the high energy tail. The gain band exhibits a continuous rise of the maximum gain value up to 300 cm^{-1} [Schi00b].

Figure 7.3 shows the excitation density dependent energy position of the edge emission and the gain maximum. At low excitation densities the gain rises on the low energy tail, in the range of localized biexcitons, which were also found to be the dominant gain mechanism in the structures containing mainly type B-islands. The pronounced blueshift of the gain maximum at highest excitation densities is induced by the saturation of the resonant gain and the appearance of a second gain process on the high energy tail of the edge emission. This behavior is assigned to state filling and population of higher excited states.

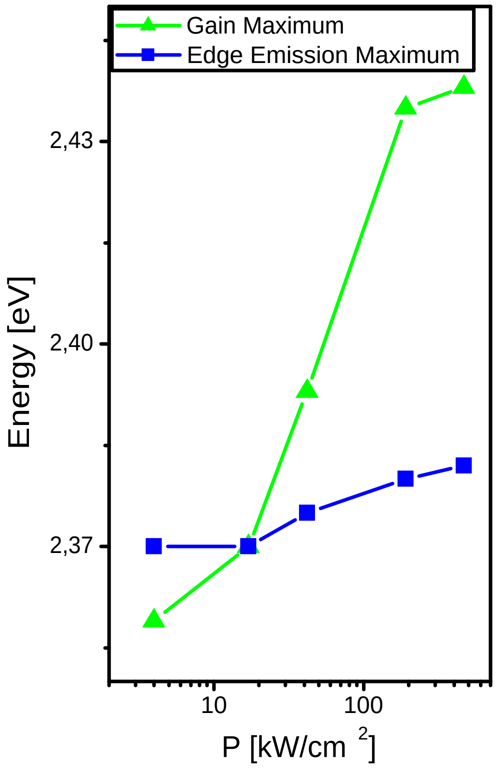

Figure 7.3: Edge emission and optical gain maximum of a ten fold stack of CdSe QD structure grown on a vicinal tilted GaAs substrate as function of the excitation density [Schi00b].

10fold stacks of CdSe QD structures on either exactly oriented substrates and on vicinal substrates show optical gain. With increasing excitation density the resonant gain saturates. A second gain process appears on the high energy tail of the edge emission line. The gain shift to higher energies is due to state filling and population of higher excited states.

8 Conclusions

The semiconductor system CdSe/ZnSe is of high interest for the fabrication of light emitting devices, either LEDs or LDs. To overcome the limitations of the II-VI materials, zero-dimensional structures are fabricated, e. g. to decrease the threshold current for laser devices.

Structural, as well as optical measurements reveal the existence of a bimodal quantum dot morphology appearing at the epitaxial growth of CdSe on pseudomorphically strained ZnSe. Two different size classes of islands are distinguished.

A. small type A-islands with a diameter less than 10 nm and a density of 10^{11}cm^{-2}.

B. large type B-islands with a diameter of 16 nm±5 nm and a density of 10^{10}cm^{-2}.

The formation process of both island classes has been analyzed by variation of growth parameters, to determine whether these formation processes are kinetically or thermodynamically controlled. Also the optical properties of these quantum dot ensembles have been investigated, too.

TEM investigations (plane view images, cross section images and CELFA analysis) revealed, that the small type A-islands are formed as Cd rich inclusions within the wetting layer. Their Cd-content increases with increasing CdSe deposition just like the Cd-content of the wetting layer itself. The density of 10^{11}cm^{-2} is independent on the CdSe deposition. Variation of substrate temperature or growth mode does not influence the formation of the type A-islands significantly, the formation process is not thermodynamically controlled. On the other hand, rough substrate surfaces, either under Cd-rich growth conditions or by using a vicinal substrate with high tilting angle, the formation of type A-islands is avoided. These parameters influence the kinetics of the growth process and show its kinetically controlled character.

The larger type B-islands are formed in a SK-process. Neither the size distribution function shows a dependence on the amount of CdSe deposited nor does the Cd-content of these islands. It remains stable at around 90% of Cd. On the other hand, the density of the islands increases with increasing CdSe coverage by more than an order of magnitude. A growth windows for strained type B-islands is also found. Two (2) MLs are the threshold coverage for the formation of the type B-islands. Three (3) MLs are the maximum thickness of the wetting layer before plastic relaxation takes place.

A reduction of the strain by replacing selenium with sulphur leads to a reduction of the type B-islands, the formation process is mainly thermodynamically controlled. Plastically relaxed islands are not influenced by this sulphur replacement, they do not recede.

The optical properties have been analyzed by temperature dependent photoluminescence, time resolved photoluminescence and photoluminescence excitation spectroscopy.

The type A-islands dominate the photoluminescence at low temperatures. With increasing CdSe coverage a shift to lower energies occurs, due to the increasing Cd-content of these shallow localized islands.

Above T=100 K a thermally activated redistribution process of excitons and carriers from shallow localized quantum dots to deep localized quantum dots appears. This leads to a redshift of ≈170 meV, which is significantly higher than predicted for the ZnSe bandedge (≈60 meV). This shift is typical for ensembles of shallow **and** deep localized quantum dots, it does not appear by the absence of the type B-islands. In this case, with increasing temperature, carriers are trapped in higher energetic states, which are given by the two-dimensional wetting layer. A quantum well like behaviour is the result.

By exitation above the ZnSe bandedge, both shallow and deep localized quantum dots show an efficient excitation. The type B-islands are exited by population through the two-dimensional inhomogeneous (Zn,Cd)Se quantum well and also by population through the shallow localized quantum dots therein. With increasing CdSe coverage, this leads to an increase of the FWHM, due to the increasing density and increasing contribution of the deep localized quantum dots to the luminescence. The type A-islands show a “hot-exciton-relaxation”, due to their quasi two-dimensional density of states.

The optical properties of the bimodal quantum dot structures are influenced more by transfer processes than by the size or density distribution.

Below T=100 K tunneling processes dominate the redistribution of carriers, the optical spectra are mainly influenced by recombination of excitons in type A-islands. Typical transfer times are ≈150 ps.

Above T=100 K thermal activated redistribution processes from type A- to type B-islands dominate. The optical spectra are mainly influenced by the optical properties of the deep localized quantum dots. The radiative lifetime of these type B-islands is ≈300 ps and shows no dependence on the temperature.

The influence of sulphur on the uncapped CdSe layers causes a reduction of the type B-islands, which results in a pronounced quantum well like behaviour of these layers.

Single dot spectroscopy on samples with type A-islands only reveal a local density of 10^9cm^{-2} on vicinal tilted GaAs substrates. This density gives the posibillity to perform real single dot spectroscopy, however an aperture of 500 nm and a FWHM of 320 μeV point to the exitation of groups of 10–100 quantum dots.

On both exactly oriented and vicinal tilted substrates ten-fold stacks of CdSe layers have been grown to investigate optical gain and stimulated emission. TEM cross section images reveal a preferred nucleation of type B-islands on surface steps, induced by stacking faults.

Both structures show gain and stimulated emission, whereas higher gain values are reached on vicinal tilted substrates, which contain mainly type B-islands.

The bimodal quantum dot ensemble reveal their high potential for light emitting devices at roomtemperature, but other field of applications are possible. By adding a cladding layer of for example (Zn,Mg)Se, active layer for lasers based on CdSe quantum dots are possible. Adding Distributed Bragg Reflectors (DBRs), VCSEL (vertical cavity surface emitting laser) structures can be realized, either for laser applications or for single polariton emitters [Pawl03].

List of abbreviations and symbols

ALE – Atomic Layer Epitaxy

BEP – Beam Equivalent Pressure

CELFA – Composition Evaluation by Lattice Fringe Analysis

CL – Cathodoluminescence

cw – continuous wave

FM – Frank-van der Merwe

FWHM – Full Width at Half Maximum

LD – Laser Diode

LED – Light Emitting Device

MBE – Molecular Beam Epitaxy

MEE – Migration Enhanced Epitaxy

ML(s) – Monolayer(s)

PL – Photoluminescence

PLE – Photoluminescence Excitation

QD – Quantum Dot

QW – Quantum Well

RF – Radio Frequency

RHEED – Reflection High Energy Electron Diffraction

sccm – standard cubic centimeter

SK – Stranski-Krastanow

TEM – Transmission Electron Microscopy

UHV – Ultra High Vacuum

VCSEL – Vertical Cavity Surface Emitting Laser

VW – Vollmer-Weber

$\boldsymbol{a_0}$ – lattice parameter

$\boldsymbol{a_S}$ – lattice parameter of the substrate layer

$\boldsymbol{a_L}$ – lattice parameter of the epitaxial layer

$\boldsymbol{\epsilon}$ – lattice mismatch

$\boldsymbol{\Theta}$ – coverage of the deposited material in MLs

$\mathbf{E_g}$ – bandgap energy

$\boldsymbol{\gamma}$ – free energy

$\mathbf{m_0}$ – electron mass

$\mathbf{m_e^*}$ – effective mass of the electron

$\mathbf{m_h^*}$ – effective mass of the hole

$\mathbf{m_{lh}^*}$ – effective mass of the light hole

$\mathbf{m_{hh}^*}$ – effective mass of the heavy hole

$\boldsymbol{\tau_{rad}}$ – radiative lifetime

List of Figures

List of Tables

Bibliography

[Bimb99] D. Bimberg, M. Grundmann, N.N. Ledentsov, *Quantum Dot Heterostructures*, (Wiley & Sons, New York 1999).

[Buda98] B. Buda, "*Molekularstrahlepitaxie und Charakterisierung von* $\mathrm{ZnS_ySe_{1-y}}$ *Quantentrogstrukturen auf GaAs(100) und GaP(100)*", Dissertation, Universität Paderborn (1998).

[Cahn68] J.W. Cahn, Trans. Metall. Soc. AIME **242**, 166 (1968).

[Chic01] S.F. Chichibu, M. Sugiyama, T. Onuma, T. Kitamura, H. Nakanishi, T. Kuroda, A. Tackeuchi, I. Ishida, H. Okumura, Appl. Phys. Lett. **79**, 4319 (2001).

[Daru97] I. Daruka and A.L. Barabazi, Phys. Rev. Lett. **79**, 3708 (1997).

[Easo95] D. Eason, J. Ren, Z. Yu, C. Huges, J.W. Cook Jr., J.F. Schetzina, N.A. El-Masry, G. Cantwell, W.C. Harsh, J. Cryst. Growth **150**, 718 (1995).

[Enge99] R. Engelhardt, U.W. Pohl, D. Bimberg, D. Litvinov, A. Rosenauer, D. Gehrtsen, J. Appl. Phys. **86**, 5578 (1999).

[Feld87] J. Feldman, G. Peter, E.O. Göbel, P. Dawson, K. Moore, C. Foxon, R.J. Elliott, Phys. Rev. Lett. **59**, 2337 (1987).

[Flac96] F. Flack, N. Samarth, V. Nikitin, P.A. Crowell, J. Shin, D.D. Avschalom, Phys. Rev. B **54** (24), R17312 (1996).

[FvdM49] F.C. Frank and J.H Van der Merwe, Proc. R. Soc. London, Ser. A **198**, 205 (1949).

[Gera96] J.M. Gerald, O. Cabrol and B. Sermage, Appl. Phys. Lett. **68**, 3123 (1996).

[Gind99b] F. Gindele, W. Langbein, J. M. Hvam, K. Leonardi, D. Hommel, H. Selke, and U. Woggon, Phys. Rev. B **60**, 8773 (1999).

[Gold85] L. Goldstein, F. Glas, J.Y. Marzin, M.N. Charasse, G. Le Roux, Appl. Phys. Lett. **47**, 1099 (1985).

[Gour89] C. Gourdon and P. Lavallard, phys. stat. sol. (b) **153**, 641 (1989).

[Grim77] H.G. Grimmeis, C. Ovren, W. Ludwig, R. Mach, J. Appl. Phys. **48**, 5123 (1977).

[Grim79] H.G. Grimmeis, C. Ovren, W. Ludwig, R. Mach, J. Appl. Phys. **50**, 6328 (1979).

[Grun96] M. Grundmann, N.N. Ledentsov, R. Heitz, D. Bimberg, V.M. Ustinov, A.Y. Egorov, M.V. Maximov, P.S. Kop'ev, Zh.I. Alferov, A.O. Kosogov, P. Werner, J. Heydenreich, U. Gödele, Proc. 8th Int. Conf. On Indium Phosphide and Related Materials (IPRM-9), IEEECatalog, 738 (1996).

[Haas91] M.A. Haase, J. Qiu, J.M. DePuydt, H. Cheng, Appl. Phys. Lett. **59**, 1272 (1991).

[Heit97a] R. Heitz, Phys. Rev. Lett. **78**(21), 4071 (1997).

[HeSi89] M. A. Herman and H. Sitter, "*Molecular Beam Epitaxy*", Springer-Verlag (1989).

[Hund01] T. Flissikowski, A. Hundt, M. Lowisch, M. Rabe and F. Henneberger, Phys. Rev. Lett. **86** (14), 3172 (2001).

[Ivan96a] S.V. Ivanov, S.V. Sorokin, P.S. Kop'ev, J.R. Kim, H.D. Jong, H.S. Park, J. Crystal Growth **159**, 1 (1996).

[Ivan96b] S.V. Ivanov, N.N. Ledentsov, M.V. Maximov, A.A. Toropov, T.V. Shubina, S.V. Sorokin, P.S. Kop'ev, H.S. Park, J.R. Kim, H.D. Jong, Semiconductors **30**, 46 (1996).

[Kato98] E. Kato, H. Hoguchi, M. Nagai, H. Okuyama, S. Kijima. A. Ishibashi, Eletr. Lett. **34** (3), 282 (1998).

[Kres98a] I.L. Krestnikov, M.V. Maximov, A.V. Sakharov, P.S. Kop'ev, Zh.I. Alferov, N.N. Ledentsov, D. Bimberg, C.M. Sotomayor Torres, J. Cryst. Growth **184/185**, 545 (1998).

[Kres99] I.L. Krestnikov, M. Strassburg, M. Caesar, A. Hoffmann, U.W. Pohl, D. Bimberg, N.N. Ledentsov, P.S. Kop'ev, Zh.I. Alferov, D. Litvinov, A. Rosenauer, D. Gehrtsen, Phys. Rev. B **60**, 8695 (1999).

[Kula99] V. D. Kulakovskii, G. Becker, K. Weigand, T. Kümmell, and A. Fordel, Phys. Rev. Lett. **82**, 1780 (1999).

[Land80] Landolt-Börnstein III, "*Zahlenwerte und Funktionen aus Naturwissenschaften und Technik*", Band 17, Teilband a,b, Springer Verlag, Berlin (1980).

[Land95] G. Landwehr and D. Hommel, phys. stat. sol. (b) **187**, 269 (1995).

[Lang75] J.S. Langer, M. Baron, H.D. Miller, Phys. Rev. A **11**, 1417 (1975).

[Lede96] N.N. Ledentsov, I.L. Krestnikov, M.V. Maximov, S.V. Ivanov, S.V. Sorokin, P.S. Kop'ev, Zh.I. Alferov, D. Bimberg, C.M. Sotomayor Torres, Appl. Phys. Lett. **69**, 1343 (1996).

[Lee00] S. Lee, J.C. Kim, H. Rho, C.S. Kim, L.M. Smith, H.E. Jackson, J.K. Furdyna and M. Dobrowolska, Phys. Rev. B **61**, R2405 (2000).

[Leon94] D. Leonard, K. Pond and P.M. Petroff, Phys. Rev. B **50**, 11687 (1994).

[Leon97] K. Leonardi, H. Heinke, K. Okhawa, D. Hommel, H. Selke, F. Gindele, U. Woggon, Appl. Phys. Lett. **71** (11), 1510 (1997).

[Lobo99] C. Lobo, R. Leon, S. Marcinkevicius, W. Yang, P.C. Sercel, X.Z. Liao, J. Zou, D.J.H. Cockayne, Phys. Rev. B **60**, 16647 (1999).

[Lüers99] D. Lüerssen, R. Bleher, H. Richter, Th. Schimmel, H. Kalt, A. Rosenauer, D. Litvinov, A. Kamilli, D. Gehrtsen, K. Ohkawa, B. Jobst and D. Hommel, Appl. Phys. Lett. **75**, 3944 (1999).

[Maki03] T. Makino, R. Andre, R. Romestain, Le Si Dang, J.-M. Gerard, M. Bartels, K. Lischka, D. Schikora, Appl. Phys. Lett. **82**, 2227 (2003).

[Merz98] J.L. Merz, S. Lee, J.K. Furdyna, J. Cryst. Growth **193**, 528 (1998).

[Naka97] S. Nakamura, G. Fasol, "*The Blue Laser Diode, GaN Based Light Emitters And Lasers*", Springer Verlag (1997).

[ODon97] K.P. O'Donnell, P.G. Middeleton, in "Properties of Wide Bandgap II-VI-Semiconductors", ed. R. Bhargava, INSPEC, emis Datareview series No. **17**, 33 (1997).

[Pawl03] A. Pawlis, "*Development and Investigation of II-VI semiconductor microcavity structures*", Thesis, Universität Paderborn (2003).

[Rabe97] M. Rabe, M. Lowisch, F. Kreller, F. Henneberger, phys. stat. sol. (b) **202**, 817 (1997).

[Rabe98] M. Rabe, M. Lowisch, F. Henneberger, J. Cryst. Growth **184/185**, 248 (1998).

[Rose98] A. Rosenauer, U. Fischer, D. Gehrtsen, A. Förster, Ultramicroscopy **72**, 121 (1998).

[Rose99] A. Rosenauer and D. Gehrtsen, Ultramicroscopy **76**, 49 (1999).

[Schä00] S. Schäfer, Diplomarbeit, Universität Karlsruhe (2000).

[Schi00a] D. Schikora, S. Schwedhelm, D.J. As, K. Lischka, D. Litvinov, A. Rosenauer, D. Gehrtsen, M. Strassburg, A. Hoffmann, D. Bimberg, Appl. Phys. Lett. **76**, 418 (2000).

[Schi00b] D. Schikora, S. Schwedhelm, I. Kudryashov, K. Lischka, D. Litvinov, A. Rosenauer, D. Gehrtsen, M. Strassburg, A. Hoffmann, D. Bimberg, J. Cryst. Growth **214/215**, 698-702 (2000).

[Schw99] S. Schwedhelm, “*Molekularstrahlepitaxie von CdSe-Quantenpunkten*”, Diplomarbeit, Universität Paderborn (1999).

[Seba02] K. Sebald, P. Michler, T. Passow, D. Hommel. G. Bacher and A. Forchel, Appl. Phys. Lett. **81**, 2920 (2002)

[Seif96] W. Seifert, N. Carlsson, M. Miller, M.-E. Pistol, L. Samuelson, L. Rheine Wallenberg, Prog. Cryst. Growth and Charact. **33**, 423 (1996).

[Seuf00] J. Seufert, D. Weigand, G. Bacher, T. Kümmell, A. Forchell, K. Leonardi and D. Hommel, Appl. Phys. Lett. **76**, 1872 (2000).

[Shch95] V.A. Shchukin, N.N. Ledentsov, P.S. Kop’ev and D. Bimberg, Phys. Rev. Lett. **75**, 2968 (1995).

[StKr37] I.N. Stranski, L. Krastanow, Sitzungsbericht der Akademie der Wissenschaften Wien, Mathematisch-naturwissenschaftliche Klasse, Abteilung II b **146**, 797 (1937).

[Stra98a] M. Strassburg, V. Kutzer, U.W. Pohl, A. Hoffmann, I. Broser, N.N. Ledentsov, D. Bimberg, A. Rosenauer, U. Fischer, D. Gehrtsen, I.L. Krestnikov, M.V. Maximov, P.S. Kop’ev, Zh.I. Alferov, Appl. Phys. Lett. **72**, 942 (1998).

[Stra98b] M. Strassburg, M. Kuttler, U.W. Pohl, D. Bimberg, Thin Solid Films **336**, 208 (1998).

[Stra00a] M. Strassburg, Th. Deniozou, A. Hoffmann, S. Rodt, V. Türck, R. Heitz, U.W. Pohl, D. Bimberg, D. Litvinov, A. Rosenauer, D. Gehrtsen, S. Schwedhelm, I. Kudryashov, K. Lischka, D. Schikora, J. Cryst. Growth **214/215**, 756 (2000).

[Stra00b] M. Strassburg, Th. Deniozou, A. Hoffmann, R. Heitz, U.W. Pohl, D. Bimberg, D. Litvinov, A. Rosenauer, D. Gehrtsen, S. Schwedhelm, K. Lischka, D. Schikora, Appl. Phys. Lett. **76**, 685 (2000).

[Stra00c] M. Strassburg, M. Dworzak, A. Hoffmann, R. Heitz, U.W. Pohl, D. Bimberg, D. Litvinov, A. Rosenauer, D. Gehrtsen, I. Kudryashov, K. Lischka and D. Schikora, phys. stat. sol. (a) **180**, 281 (2000).

[Stra02a] M. Strassburg, J. Christen, M. Dworzak, R. Heitz, A. Hoffmann, M. Bartels, K. Lischka, D. Schikora, phys. stat. sol. (b) **229**, 529 (2002).

[Stra02b] M. Strassburg, M. Dworzak, H. Born, R. Heitz and A. Hoffmann, M. Bartels, K. Lischka and D. Schikora, J. Christen, Appl. Phys. Lett. **80** (3), 473 (2002).

[Stra02c] M. Strassburg, "*Energietransfer von Exzitonen in ZnCdSe Quantenpunkt Ensembles*", Dissertation, Technische Universität Berlin (2002).

[Tsao93] J. Y. Tsao, "*Materials Fundamentals of Molecular Beam Epitaxy*", Academic Press Inc. (1993).

[VoWe26] M. Volmer and A. Weber, Z. Physik. Chem. **119**, 277 (1926).

[Waag97] A. Waag, F. Fischer, K. Schüll, T. Baron, H.J. Lugauer, Th. Litz, U. Zehnder, W. Ossau, T. Gerhard, M. Keim, G. Reuscher and G. Landwehr, Appl. Phys. Lett. **70** (3), 280 (1997).

[Zink92] M. Zinke-Allmang, L.C. Feldman and M.H.Grabow, Surf. Sci. Reports **16**, 377 (1992).

Acknowledgements

It is not possible to thank all the people who deserve it. But never the less, there are some who must be mentioned right here.

First of all I would like to thank Prof. Dr. K. Lischka for giving me the opportunity to work in such an excellent research group. My gratitude also goes to Dr. D. Schikora for his guidance during my Ph.D. thesis.

I would like to thank Apl. Prof. Dr. D.J. As for the discussions and his help on optical problems in II-VI semiconductors.

Moreover I would like to thank Dr. M. Strassburg of the university of Berlin for the optical characterization during the collaboration.

It's an absolute must to thank the optoelectronics staff namely I. Zimmermann, S. Igges and B. Volmer for their technical support. (They do much more than this!) If you have any question, just ask them, they're almost incredible.

Incredible are also my fellow Ph.D. students U. Köhler, A. Khartchenko, O. Husberg, S.F. Li, S. Potthast, S. Preuss, C. Arens and J. Schörmann. I would like to thank you for all the discussions and the barbecues. A special one goes to A. Pawlis, we have been the best team in MBE, nearly unable to top. There is nothing we cannot repair (and destroy before, that's for sure). I know you'll all miss me like hell (o.k. not me but my burgers at the barbecues). "*You guys are crazy!*"

I would like to thank R. Winterberg for a few hundred liters of coffee, without you some days work would not be possible.

My "*very special*" thanks goes to the people on the fourth floor for all the water they shared with us. Next time please use a bucket, just take care of the people working below you.

I am quite not able to express my thank to the HRZ for the large bandwidth I needed sometimes and for all the computer programs we used. Life would be so boring without blue screens and funny error messages.

There's been a world outside university, so I have to thank a lot of other people too.
My family for encouraging me during my work.
Mia, Lina, Luca, Judith and Thomas for their chaos at home, for an endless number of dinners, even if I have to cook them myself sometimes. You showed me that there is more than working, eating and sleeping.

This work was supported by the Volkswagen-Stiftung Project-No. I/75 591.

List of publications

A. Kaschner, M. Strassburg, A. Hoffmann, C. Thomsen, *M. Bartels*, K. Lischka, D. Schikora
Temporal evolution of resonant Raman-scattering in ZnCdSe quantum dots
Appl. Phys. Lett. **76**, 2662-2664 (2000).

D.J. As, T. Frey, *M. Bartels*, K. Lischka, R. Goldhahn, S. Shokhovets, A. Tabata, J.R.L. Fernandez, J.R. Leite
MBE growth of $\mathrm{Al_yGa_{1-y}N/GaN}$ *heterostructures – structural, vibrational and optical properties*
J. Cryst. Growth **230**, 421-425 (2001).

D.J. As, T. Frey, *M. Bartels*, A. Khartchenko, D. Schikora, K. Lischka, R. Goldhahn, S. Shokhovets
Optical properties of MBE grown cubic AlGaN epilayers and AlGaN/GaN quantum well structures
MRS Symp. Proc. Vol. 639, G5.9 (2001).

T. Frey, D.J. As, *M. Bartels*, A. Pawlis, K. Lischka, A. Tabata, J.R.L. Fernandez, M.T.O. Silva, J.R. Leite, C. Haug, R. Brenn
Structural and vibrational properties of MBE grown cubic (Al,Ga)N/GaN heterostructures
J. Appl. Phys. **89**, 2631-2634 (2001).

D. Litvinov, A. Rosenauer, D. Gehrtsen, I. Kudryashov, *M. Bartels*, D. Schikora
Correlation between nominal CdSe content, real Cd concentration and growth parameters in CdSe quantum dot structures
J. Cryst. Growth **244**, 483 (2001).

M. Strassburg, M. Dworzak, H. Born, R. Heitz, A. Hoffmann, *M. Bartels*, K. Lischka, D. Schikora, J. Christen
Lateral redistribution of excitons in CdSe/ZnSe quantum dots
Appl. Phys. Lett. **80**, 473-475 (2002).

M. Strassburg, J. Christen, M. Dworzak, R. Heitz, A. Hoffmann, *M. Bartels*, K. Lischka, D. Schikora
Analysis of Quantum Dot Formation and Exciton Localisation in the (Zn,Cd)(S,Se) System
phys. stat. sol. (b) **229**, No. 1, 529-532 (2002).

T. Makino, R. Andre, J.-M. Gerard, R. Romestain, Le Si Dang, *M. Bartels*, K. Lischka, D. Schikora
Effect of growth conditions on optical properties of CdSe/ZnSe single quantum dots
cond-mat/0211307 (2002).

T. Makino, R. Andre, J.-M. Gerard, R. Romestain, Le Si Dang, *M. Bartels*, K. Lischka, D. Schikora
Single quantum dot spectroscopy of CdSe/ZnSe grown on vicinal GaAs substrates
Appl. Phys. Lett. **82**, 2227-2229 (2003).

T. Makino, R. Andre, J.-M. Gerard, R. Romestain, Le Si Dang, *M. Bartels*, K. Lischka, D. Schikora
Effect of growth conditions on optical properties of CdSe/ZnSe single quantum dots
Physica E **17**, 97-98 (2003).

I.C. Robin, R. Andre, Le Si Dang, H. Mariette, S. Tatarenko, J.M. Gerard, K. Kheng, F. Tinjod, *M. Bartels*, K. Lischka, D. Schikora
How to avoid non-radiative escape of excitons from quantum dots?
submitted to phys. stat. sol.